

# Energy Landscapes for the Quantum Approximate Optimisation Algorithm

Choy Boy<sup>1</sup> and David J. Wales<sup>1</sup>

<sup>1</sup>*Yusuf Hamied Department of Chemistry, University of Cambridge,  
Lensfield Road, Cambridge, CB2 1EW, United Kingdom*

Variational quantum algorithms (VQAs) have demonstrated considerable potential in solving NP-hard combinatorial problems in the contemporary near intermediate-scale quantum (NISQ) era. The quantum approximate optimisation algorithm (QAOA) is one such algorithm, used in solving the maximum cut (Max-Cut) problem for a given graph by successive implementation of  $L$  quantum circuit layers within a corresponding Trotterised ansatz. The challenge of exploring the cost function of VQAs arising from an exponential proliferation of local minima with increasing circuit depth has been well-documented. However, fewer studies have investigated the impact of circuit depth on QAOA performance in finding the correct Max-Cut solution. Here, we employ basin-hopping global optimisation methods to navigate the energy landscapes for QAOA ansätze for various graphs, and analyse QAOA performance in finding the correct Max-Cut solution. The structure of the solution space is also investigated using discrete path sampling to build databases of local minima and the transition states that connect them, providing insightful visualisations using disconnectivity graphs. We find that the corresponding landscapes generally have a single funnel organisation, which makes it relatively straightforward to locate low-lying minima with good Max-Cut solution probabilities. In some cases below the adiabatic limit the second lowest local minimum may even yield a higher solution probability than the global minimum. This important observation has motivated us to develop broader metrics in evaluating QAOA performance, based on collections of minima obtained from basin-hopping global optimisation. Hence we establish expectation thresholds in elucidating useful solution probabilities from local minima, an approach that may provide significant gains in elucidating reasonable solution probabilities from local minima.

## I. INTRODUCTION

The initial setback of implementing practical quantum algorithms utilising the quantum phase estimation (QPE) architecture onto current-day near intermediate-scale quantum (NISQ) devices [1–3], which typically possess short decoherence times [4] and significant quantum noise [5], has prompted the rapid development of variational quantum algorithms (VQAs) with shorter quantum circuit depths [6–8]. VQAs typically operate within a hybrid classical-quantum optimisation framework [9], where an initial quantum state is evolved by a parameterised circuit ansatz on a quantum device. After the final evolved wavefunction is measured, a classical optimiser evaluates the cost function from the measurement and subsequently suggests new parameters that are fed back into the parameterised quantum circuit. This interface between classical and quantum computers iterates until a suitable convergence criterion is attained. VQAs have proved to be surprisingly robust in tackling various sources of noise attributed to NISQ devices, such as decoherence [10] and depolarisation [11]. These properties are ascribed to the innate variational nature acting as a parametric lever, which can be flexibly adjusted even under noisy environments [12]. Coupled with the recent advances in error-mitigation methods [13–15], it is anticipated that VQAs will enable the realisation of practical quantum advantage before the advent of fault-tolerant devices equipped with error-correction protocols [16].

The quantum approximate optimisation algorithm (QAOA) is a VQA that monotonically improves in performance as the number of quantum circuit layers in the ansatz increases [17]. Variational quantum eigensolver (VQE) algorithms typically utilise the global minimisation of the cost landscape directly as

the solution of interest [18]. In contrast, QAOA uses the resulting final wavefunction to obtain approximate solutions based on the states in the computational basis with the highest frequency when measurement after circuit evolution is carried out. Hence QAOA is a particularly attractive algorithm for solving combinatorial optimisation problems, such as Max-Cut [19], with promising applications in portfolio optimisation [20] and chemistry [21, 22].

The expansion of VQAs has also motivated the study of their potential shortcomings in solving practical large-scale problems from a software perspective. In particular, for various VQA ansätze there is an exponential growth in the barren plateau problem as the number of qubits and circuit layers required to encode a given problem increases [23–25]. Recently, more insight has also been gained into the challenges of exploring the cost landscapes of VQAs that arise from a proliferation in the number of local minima and other stationary points as the complexity of the problem increases [26, 27]. However, further analysis of the organisation of the global cost landscapes of VQAs, and how this structure impacts the quality of the solutions obtained, is needed, especially for QAOA [28, 29].

Here, we seek to address these gaps in understanding using the well-established theory and associated computational methodology of molecular energy landscapes [30, 31]. We characterise the cost optimisation landscapes of QAOA for various weighted and unweighted graphs in solving the Max-Cut problem using basin-hopping global optimisation methods [32–34] to locate global minima, and discrete path sampling [35, 36] to create connected databases of minima and the transition states that connect them. Recently, energy landscape techniques have demonstrated considerable utility for quantum computing in the analysis of hardware-efficient ansätze for the VQE algo-

rithm [37], and optimisation of electronic wavefunctions in a combined discrete space of operators and continuous parameter amplitudes [38]. Our new results for QAOA show that the solution landscapes below the adiabatic limit generally possess single-funnelled structures associated with self-organising systems where locating the global minimum is relatively straightforward [30, 39, 40]. Furthermore, we find that local minima sufficiently close in energy to the global minimum may also exhibit good solution probabilities for the Max-Cut problem. In some instances, the second lowest minimum has a higher solution probability than the global minimum, highlighting the importance of studying the VQA solution landscape globally. This observation leads us to introduce metrics that take into account the distribution of minima in evaluating the performance and robustness of QAOA. We also utilise the convex hull of the solution space in estimating expectation cut-offs for the location of local minima with reasonable solution probabilities. We hope that these techniques can advance the feasibility of implementing QAOA for problems with numerous local minima in noisy environments.

## II. METHODOLOGY

Given an undirected graph  $G = (V, E)$ , with weights  $w_{ij}$  assigned to edges  $e_{ij} \in E$  for connected vertices  $i, j \in V$ , the Max-Cut problem seeks to partition  $V$  into two distinct sets such that the sum of weights between the two sets is maximised. If  $w_{ij} = 1$  for all  $e_{ij}$ , then  $G$  is said to be an unweighted graph; otherwise  $G$  is a weighted graph. It follows that the Max-Cut problem can be mapped to a two-spin Ising-type cost Hamiltonian  $\hat{H}_C$  corresponding to  $N$  implementable qubits:

$$\hat{H}_C = \frac{1}{2} \sum_{e_{ij} \in E} w_{ij} (Z_i \otimes Z_j), \quad (1)$$

where the states  $|s\rangle = \{|\alpha\rangle, |\beta\rangle\}^{\otimes N}$  encode the desired solution strings to the Max-Cut problem, with  $|\alpha\rangle = |0\rangle$  if and only if  $|\beta\rangle = |1\rangle$ , and vice versa. Thus, the aim of QAOA is to approximate the ground-state energy or the lowest eigenvalue of  $\hat{H}_C$  via a suitable ansatz with unitary operator  $\hat{U}(\theta)$  to evolve an initial state  $|\psi_0\rangle$ , and subsequently use the final evolved state  $|\Psi(\theta)\rangle = \hat{U}(\theta)|\psi_0\rangle$  to approximate  $|s\rangle$ . This objective can be achieved on a quantum device by performing a certain number of shots per experiment and measuring all qubits in the computational basis, taking the state possessing the greatest number of shots to best approximate  $|s\rangle$  for that experiment. We seek to simulate this procedure classically by considering the probability of measuring the state  $|s\rangle$  in the computational basis,  $p(|s\rangle)$ :

$$p(|s\rangle) = |\langle s | \Psi(\theta) \rangle|^2. \quad (2)$$

The objective function to be minimised by the classical computer is the expectation of  $\hat{H}_C$ ,  $\langle \hat{H}_C \rangle$ :

$$\langle \hat{H}_C \rangle = E(\theta) = \langle \psi_0 | \hat{U}^\dagger(\theta) \hat{H}_C \hat{U}(\theta) | \psi_0 \rangle. \quad (3)$$

The QAOA ansatz with parameters  $\theta = \{\gamma, \delta\}$  can be assembled as a Trotterised variational schedule, comprising a cost circuit layer with unitary operator  $\hat{U}_C(\gamma)$ , followed by a mixer circuit layer with unitary operator  $\hat{U}_M(\delta)$  up to a circuit depth  $L$ :

$$|\Psi(\gamma, \delta)\rangle = \prod_{l=1}^L \hat{U}_M(\delta_l) \hat{U}_C(\gamma_l) |\psi_0\rangle, \quad (4)$$

where  $|\psi_0\rangle = |+\rangle^{\otimes N}$  is the state encoding for all possible partitions of  $V$  with equal probability. The cost layer encapsulating  $\hat{H}_C$  can be compiled as a sequence of two-qubit parameterised  $R_{zz}$  quantum gates for qubits  $q_i$  and  $q_j$ , with  $\gamma$  scaled based on the weights of  $e_{ij}$ :

$$\begin{aligned} \hat{U}_C(\gamma) &= e^{-i\gamma \hat{H}_C} \\ &= \prod_{e_{ij} \in E} R_{zz}(-w_{ij}\gamma). \end{aligned} \quad (5)$$

The mixer layer performs a time-evolution of the mixer Hamiltonian  $\hat{H}_M = -\sum_{i=1}^N X_i$ , which anti-commutes with  $\hat{H}_C$  and has  $|\psi_0\rangle$  as an eigenvector. The mixer layer can be realised as a parallelisation of single-qubit parameterised  $R_x$  quantum gates:

$$\begin{aligned} \hat{U}_M(\delta) &= e^{-i\delta \hat{H}_M} \\ &= \bigotimes_{i=1}^N R_x(2\delta). \end{aligned} \quad (6)$$

It has been shown that QAOA conforms to the adiabatic theorem, i.e. for  $L \rightarrow \infty$  the final evolved state  $|\Psi(\theta)\rangle$  converges exactly to the ground state of  $\hat{H}_C$ , and thus gives the optimal  $p(|s\rangle)$  [17]. In practice, such an implementation is unfeasible in the NISQ regime, hence we are interested in considering  $L_{ad}$  for a given system, defined as the minimum number of circuit layers required to reach the adiabatic limit, assuming that  $L_{ad}$  can be attained. As we will demonstrate in our analysis of the energy landscapes of QAOA, it is also important to distinguish  $L_{ad}$  from  $L_{min}$ , where  $L_{ad} \geq L_{min}$ . Here,  $L_{min}$  is the minimum number of layers needed to achieve the maximum  $p(|s\rangle)$  in the corresponding global minimum. Local minima with lower  $p(|s\rangle)$  may be present due to underparametrisation of the circuit ansatz, and hence a less thorough exploration of states in the Hilbert space may be sufficient to obtain a useful solution. We hypothesise that the exponential increase in the number of local minima is attributable to circuit ansätze with  $1 \leq L \leq L_{min}$  layers. The behaviour of local minima may vary for  $L_{min} < L \leq L_{ad}$  layers if  $L_{min} < L_{ad}$ , and we observe for various graphs that the number of local minima may increase first before decreasing to the adiabatic limit, or instead decrease monotonically.

For each graph considered and  $L$ , we generate an initial set of minima via basin-hopping global optimisation [32–34] using the GMIN program [41]. The analytic gradients of the parameterised rotation gates

were calculated via the parameter-shift rule [42] (see **Appendix A** for more details):

$$\frac{\partial E(\boldsymbol{\theta})}{\partial \theta_i} = \frac{1}{2} \left[ E\left(\boldsymbol{\theta} + \frac{\pi}{2} \mathbf{e}_i\right) - E\left(\boldsymbol{\theta} - \frac{\pi}{2} \mathbf{e}_i\right) \right]. \quad (7)$$

Local minimisation for the basin-hopping steps employed a limited-memory Broyden [43], Fletcher [44], Goldfarb [45], Shanno [46] (L-BFGS) procedure [47, 48] equipped with the Metropolis criterion for accepting/rejecting steps [49]. The resulting minima were then employed as the starting points for construction of a kinetic transition network [50–52]. Discrete path sampling [35, 36] (DPS) was used via connection attempts for selected minima pairs with final states  $|\Psi(\boldsymbol{\theta}_\mu)\rangle$  and  $|\Psi(\boldsymbol{\theta}_\nu)\rangle$ . The doubly-nudged [53, 54] elastic band [55–58] approach was used to locate candidates for accurate transition state refinement by hybrid eigenvector-following [59–61]. The missing connection algorithm [62] was used to select pairs of minima to fill in the gaps in incomplete pathways via Dijkstra’s shortest path algorithm [63] combined with a distance metric based on the state overlap between local minima,  $S_{\mu\nu}$ :

$$S_{\mu\nu} = 1 - |\langle \Psi(\boldsymbol{\theta}_\mu) | \Psi(\boldsymbol{\theta}_\nu) \rangle|. \quad (8)$$

Any new minima are added to the database along with the transition states and connection information. The resulting cost landscapes can be visualised using disconnectivity graphs, where the local minima are segregated into disjoint sets for regular thresholds in the energy [39, 64]. In these graphs, the bottom of a branch corresponds to the energy of a local minimum, and the branches are joined when the corresponding minima can interconvert via a pathway below the given threshold. Visualisation of the energy landscape can be further enhanced by colouring each minimum with the corresponding probability of finding the correct Max-Cut solution; we find this construction especially useful in comparing the solution landscapes as  $L$  varies.

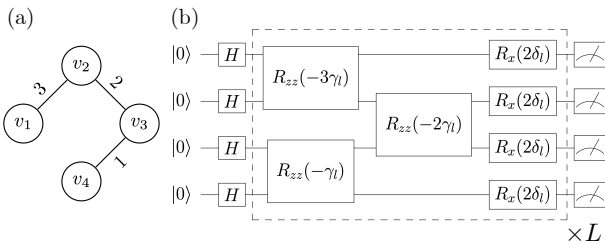


FIG. 1. **(a) (left)** Weighted graph  $G_1$  encoded with four qubits. **(b) (right)** Corresponding QAOA ansatz for  $G_1$ .

As an example, consider the weighted graph  $G_1$  with four vertices (**Fig. 1a**), where the Max-Cut problem can be encoded as a four-qubit QAOA ansatz with varying  $L$  (**Fig. 1b**). We note that although the ansatz cost circuit layer can be compiled in numerous ways, the arrangement in **Fig. 1b** is ideal in reducing the overall circuit depth. This ordering does not require swap gates to permute non-neighbouring qubits corresponding to their respective edges, which is an important consideration when transpiling QAOA

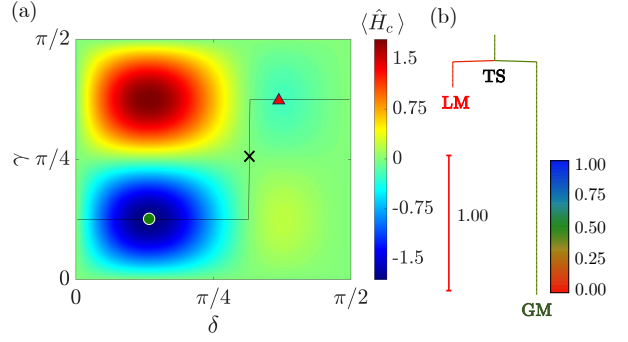


FIG. 2. **(a) (left)** Contour plot of  $\langle \hat{H}_C \rangle$  for graph  $G_1$  and its QAOA ansatz with  $L = 1$  against the parameters  $\gamma$  and  $\delta$ . The solid line depicts the minimum of each vertical slice of the contour plot, with the global minimum (**GM**, green circle), local minimum (**LM**, red triangle) and the transition state connecting them (**TS**, black cross) situated on the pathway that is also plotted. **(b) (right)** Corresponding disconnectivity graph of the contour plot in **Fig. 2a**, with both the **GM** and **LM** coloured (grayscale) based on their respective probabilities of obtaining the correct Max-Cut solution of  $|\alpha\beta\alpha\beta\rangle$ .

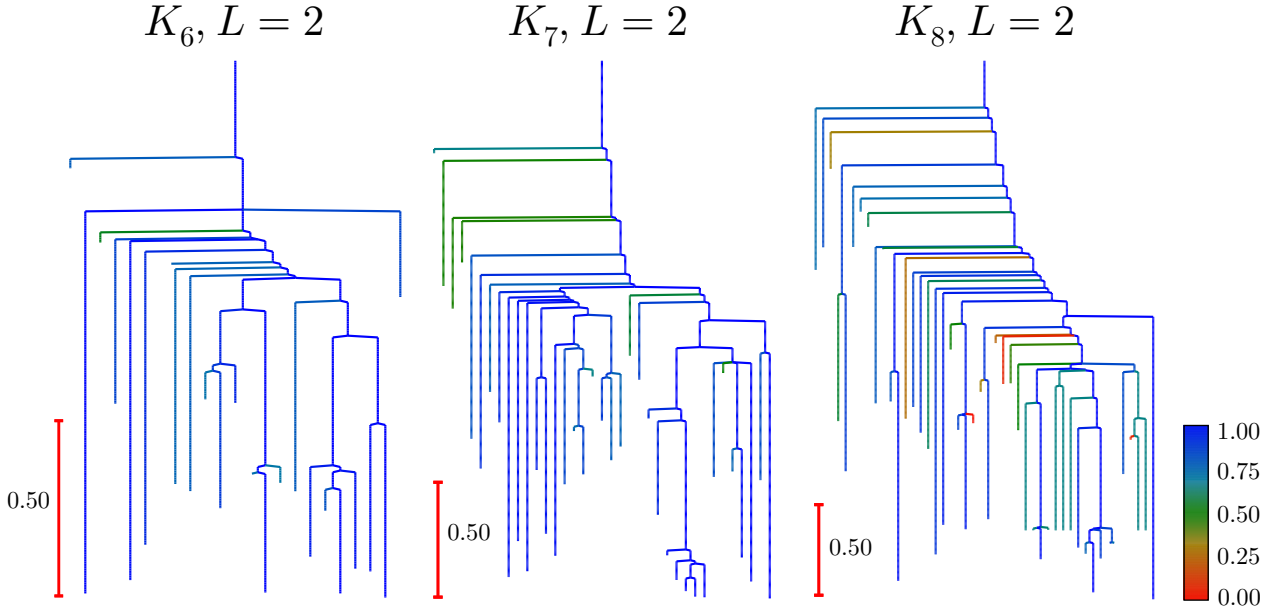
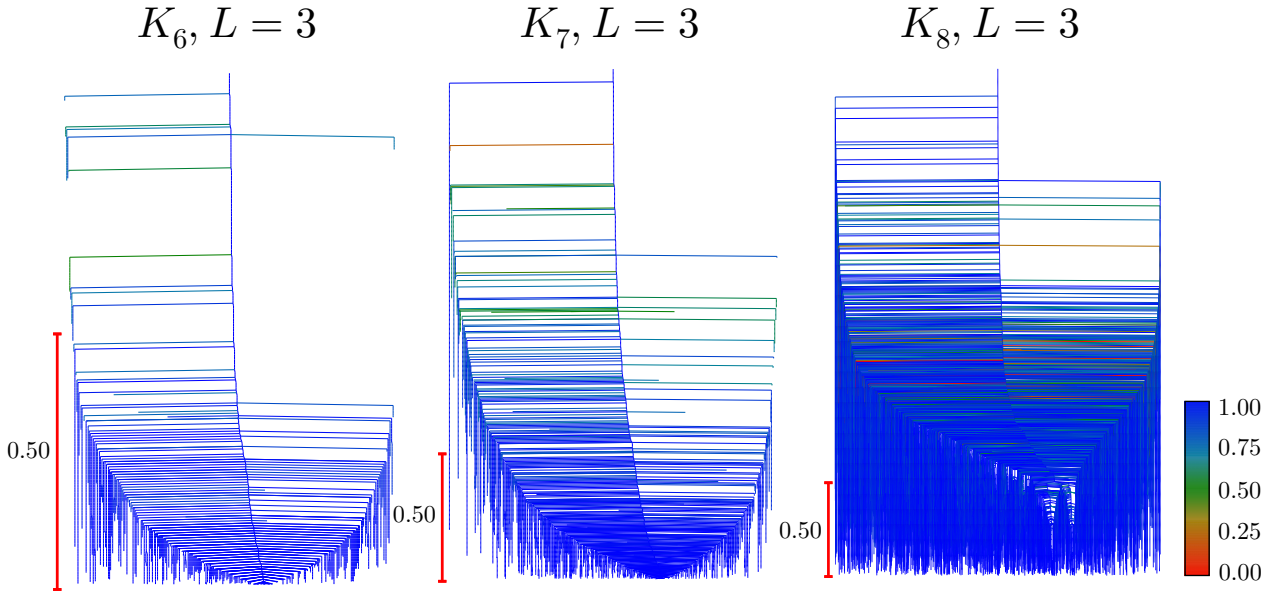
onto planar superconducting processors [65]. The cost landscape of the  $L = 1$  circuit ansatz features a global and a local minimum connected by a transition state (**Fig. 2a**), and the corresponding disconnectivity graph is shown in **Fig. 2b**, where the branches are coloured with the probabilities of finding the state  $|\alpha\beta\alpha\beta\rangle$ , which corresponds to the Max-Cut solution of  $G_1$ .

### III. RESULTS

#### A. Complete unweighted graphs

We begin by examining the QAOA circuit ansätze for the complete unweighted graph series  $K_N$  from  $N = 3$  to  $N = 8$  and from  $L = 1$  to  $L = 3$ , where each vertex is connected to every other vertex with unit weight. It follows that the Max-Cut solution of  $K_N$  is the set of all possible tensor product permutations of  $\lfloor N/2 \rfloor$  number of  $|\alpha\rangle$  states and  $\lceil N/2 \rceil$  number of  $|\beta\rangle$  states: thus the total number of Max-Cut solutions for odd  $N$  is  $2N! / \{\lfloor N/2 \rfloor! \lceil N/2 \rceil!\}$ , and for even  $N$   $N! / \{2(N/2)!\}$  solutions.

**Table I** summarises the number of minima  $M$  and the highest correct Max-Cut probability (HCMP) from the collections of minima obtained via basin-hopping global optimisation for  $L = 1$  to  $L = 3$ . The complete graphs with odd  $N$  generally possess higher HCMPs than their even counterparts, mainly due to their greater number of accepted Max-Cut solutions that contribute to their corresponding probabilities. We also find that although for  $K_6$  to  $K_8$  the expected exponential increase in  $M$  is observed as  $L$  increases, for  $K_5$  there was a decrease in the number of minima from  $L = 2$  to  $L = 3$ , leading to a simplification in the energy landscape from  $L_{min} = 2$  to  $L_{ad} = 3$ . Looking at the disconnectivity graphs of  $K_6$  to  $K_8$  for

FIG. 3. Disconnectivity graphs of  $K_6$ ,  $K_7$  and  $K_8$  for  $L = 2$ .FIG. 4. Disconnectivity graphs of  $K_6$ ,  $K_7$  and  $K_8$  for  $L = 3$ .

$L = 2$  (**Fig. 3**) and  $L = 3$  (**Fig. 4**), we observe that the majority of the local minima generally possess very high correct Max-Cut probabilities, particularly those closer to the global minimum, especially as  $L$  and  $M$  increase. The well-funnelled organisation of the landscape also becomes more apparent as  $L$  increases, and this structure is expected to outweigh the challenges associated with solving the Max-Cut problem for higher  $N$ , particularly for  $K_8$ , where local minima with low probabilities are increasingly interspersed with other local minima corresponding to higher probabilities.

To further evaluate the performance of QAOA ansätze for various  $L$  based on the databases of min-

ima and their respective Max-Cut probabilities and  $\langle \hat{H}_C \rangle$  values, we introduce the weighted average metric  $F$ :

$$F = \frac{1}{M|\langle \hat{H}_C \rangle_{min}|} \sum_{m=1}^M |\langle \hat{H}_C \rangle_{min} - \langle \hat{H}_C \rangle_m| [1 - p_m(|s\rangle)], \quad (9)$$

where  $\langle \hat{H}_C \rangle_{min}$  is the  $\langle \hat{H}_C \rangle$  value of the global minimum. This formulation of  $F$  is advantageous for two reasons. First, it distinguishes circuit ansätze with  $L_{ad}$  and  $L_{min}$  layers, since for  $L_{ad}$ ,  $F = 0$  because only the global minimum is present, compared to  $L_{min}$  where other local minima with lower Max-Cut prob-



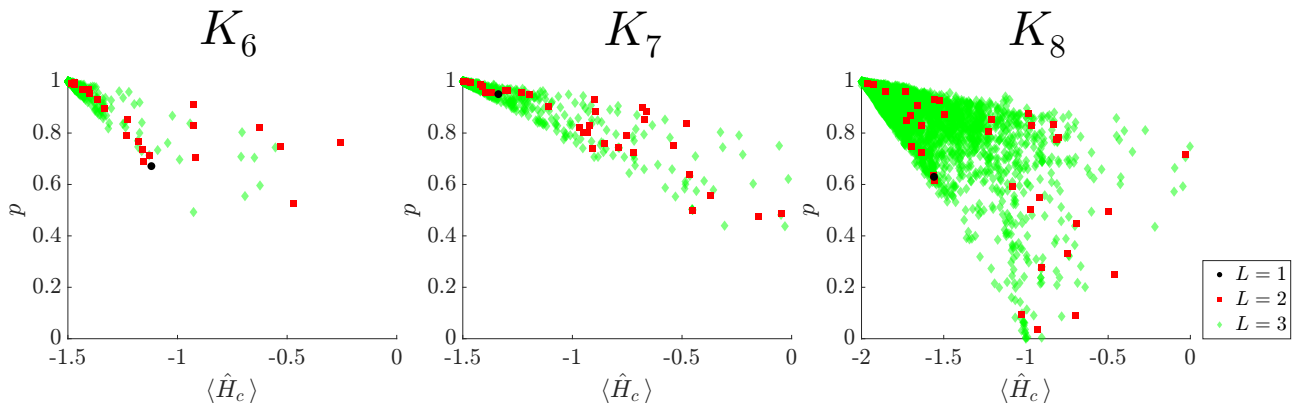


FIG. 5. Scatter plots of probabilities of the correct Max-Cut solutions against  $\langle \hat{H}_C \rangle$  for individual minima of graphs  $K_6$ ,  $K_7$  and  $K_8$  for  $L = 1$  (black circle),  $L = 2$  (red square) and  $L = 3$  (green diamond).

TABLE I. Number of minima  $M$  (top value) and the highest correct Max-Cut probability (HCMP) (bottom value) for graphs  $K_3$  to  $K_8$  with varying  $L$  obtained from basin-hopping global optimisation. For the case of  $K_8$  and  $L = 3$ , the HCMP is not equal to the maximum value of 1, and the number of decimal places used for all HCMPs is chosen to be the same as this case for ease of comparison.

Graph	$L = 1$	$L = 2$	$L = 3$
$K_3$	1 1.000000	1 1.000000	1 1.000000
$K_4$	1 0.739106	1 1.000000	1 1.000000
$K_5$	1 0.975990	4 1.000000	1 1.000000
$K_6$	1 0.671340	23 0.994239	324 1.000000
$K_7$	1 0.951350	37 0.999619	598 1.000000
$K_8$	1 0.629727	46 0.991483	3418 0.999997

abilities are present. Second,  $F$  reflects the contribution of minima for circuit ansätze with  $L < L_{min}$  more accurately, since it is possible for minima with lower  $\langle \hat{H}_C \rangle$  values, including the global minimum, to possess lower Max-Cut probabilities than their counterparts with higher  $\langle \hat{H}_C \rangle$  values. As  $L$  increases, a decrease in the value of  $F$  can generally be interpreted as an improvement in QAOA performance, since it corresponds to an increase in the proportion of local minima with better probabilities. However, the converse situation, where  $F$  increases as  $L$  increases, may not necessarily signify a drop in QAOA performance, as the well-funnelled organisation of the cost landscape, as well as the guarantee of obtaining a better Max-Cut probability, may outweigh the trade-off in obtaining a lower proportion of local minima with relatively good probabilities. Nevertheless, we propose choosing circuit ansätze with  $L$  layers that feature sufficiently low values of  $F$  when simulating QAOA on noisy quantum devices, as choosing circuits with higher  $L$  may also increase the impact of quantum gate and qubit decoherence noise.

TABLE II. The weighted average metric  $F$  for graphs  $K_5$  to  $K_8$  of varying  $L$ .

Graph	$L = 1$	$L = 2$	$L = 3$
$K_5$	0.002276	0.067219	0.000000
$K_6$	0.083438	0.060651	0.007907
$K_7$	0.005269	0.119087	0.026351
$K_8$	0.081604	0.190701	0.038062

Analysing the  $F$  values for  $K_5$  to  $K_8$  (Table II), we observe that for  $K_5$ ,  $F = 0$  for  $L_{ad} = 3$ , differentiating it from  $L_{min} = 2$ , as expected. Interestingly, with the exception of  $K_6$ ,  $F$  appears to increase for  $L = 2$  before decreasing for  $L = 3$ . The increase in  $F$  can mainly be attributed to the general increase in the number of local minima for  $L = 2$  with comparably lower probabilities than that of the single global minimum for  $L = 1$ . This trend is evident in the scatter plots of the probabilities of the correct Max-Cut solution against  $\langle \hat{H}_C \rangle$  for the databases of minima for varying  $L$  (Fig. 5). The somewhat triangular convex hull of the solution space,  $C_s$ , seems to become better defined with the transition from  $L = 2$  to  $L = 3$ . We also see a proliferation of local minima towards the apex of the global minimum, which would explain the observed subsequent decrease in  $F$ . Thus, a choice of  $L = 3$  would be adequate for solving the Max-Cut problem for graphs  $K_5$  to  $K_8$  based on their  $F$  values.

### B. 3-regular unweighted graphs

Next, we analysed all connected 3-regular unweighted graphs with six and eight vertices [66] from  $L = 1$  to  $L = 4$ , labelled **6a–8e**, respectively (Fig. 6). In terms of the number of minima obtained from basin-hopping runs, the 3-regular graphs generally possess lower  $M$  values than the complete graphs of  $K_6$  and  $K_8$ , particularly for graphs with eight vertices (Table III). For graph **6b**, starting from  $L = 1$  its QAOA ansatz gives rise to more than one minimum, which subsequently produces a more rapid increase in  $M$  compared to its counterpart **6a**. This phenomenon

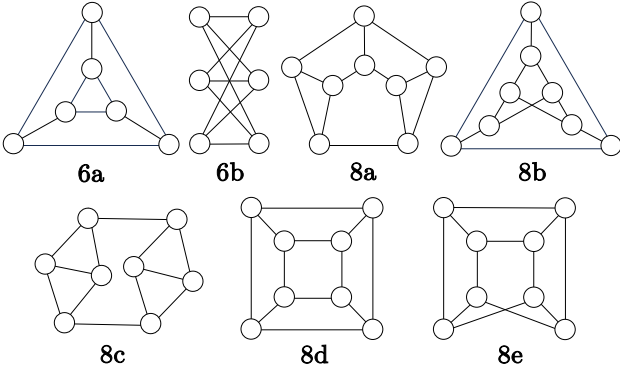


FIG. 6. 3-regular unweighted graphs **6a–8e** investigated in this study.

TABLE III. Number of minima  $M$  (top value), HCMPs (middle value) and  $F$  (bottom value) for graphs **6a–8e** of varying  $L$  obtained from basin-hopping global optimisation. HCMPs with asterisks indicate that they correspond to the next highest local minimum rather than the global minimum.

Graph	$L = 1$	$L = 2$	$L = 3$	$L = 4$
	1	5	23	145
<b>6a</b>	0.400816 0.254240	0.720917 0.224891	0.933445* 0.167129	0.996304 0.093993
	3	20	191	1451
<b>6b</b>	0.274835 0.772861	0.659823 0.615867	0.915348 0.510817	0.978625 0.340108
	1	4	16	83
<b>8a</b>	0.142701 0.427166	0.349371 0.363476	0.616672 0.497637	0.748746 0.428079
	1	4	15	97
<b>8b</b>	0.232056 0.355057	0.420045* 0.325065	0.638057 0.426828	0.767138 0.380643
	1	4	18	82
<b>8c</b>	0.077352 0.516636	0.182753 0.560946	0.536762 0.519856	0.701246 0.429701
	1	6	31	151
<b>8d</b>	0.186302 0.500506	0.520680 0.360078	0.871573 0.258910	0.972013 0.141219
	1	4	15	110
<b>8e</b>	0.321737 0.286668	0.574918* 0.241691	0.769975 0.302882	0.918878* 0.300042

can largely be attributed to the relatively more complex analytic expression of  $\langle \hat{H}_C \rangle$  with the  $L = 1$  circuit ansatz [67] for **6b**. Another interesting pair of graphs is **8d** and **8e**, where, although their  $L = 1$  analytic expressions of  $\langle \hat{H}_C \rangle$  are identical and thus give rise to the same  $\langle \hat{H}_C \rangle_{\min}$  value [67], we find that the trends of  $M$  and HCMPs for higher  $L$  are markedly different. Although the 3-regular series of graphs give rise to lower  $M$  for similar  $L$ , and hence somewhat simpler energy landscapes compared to their complete graph counterparts, their HCMPs are also comparatively lower, hence requiring a greater  $L$  to achieve a sufficiently high HCMP. In some cases, the HCMPs were derived not from the global minimum, but from the next highest local minimum. (See **Appendix B**

detailing the differences in Max-Cut probabilities and  $\langle \hat{H}_C \rangle$  values between the two minima for these cases.) This phenomenon appears sporadically without much predictability, most notably for graph **8e**, where the HCMP corresponds to the next highest local minimum for  $L = 2$  and  $L = 4$ . Overall, these observations further underline the importance of evaluating QAOA performance based on the correct Max-Cut probabilities of individual minima independently alongside their  $\langle \hat{H}_C \rangle$  values.

The distributions of minima for the 3-regular graphs with varying  $L$  differ significantly from their complete graph counterparts (**Fig. 7**). We observe that the convex hulls of the 3-regular graphs tend to take on a more compact shape, with greater correlation between the  $p(|s\rangle)$  and  $\langle \hat{H}_C \rangle$  values for the individual minima. However, for graphs **8a**, **8b** and **8e** there is a notable absence of minima with intermediate  $p(|s\rangle)$  and  $\langle \hat{H}_C \rangle$  values, particularly for higher  $L$ . This structure is also reflected in their disconnectivity graphs (refer to **Appendix C** for the disconnectivity graphs of **6a–8e**). Another major difference of the 3-regular graphs is the much reduced energy differences between minima with low proximity to the global minimum and their connected transition states, producing more streamlined and single-funnelled disconnectivity graphs than for  $K_6$  and  $K_8$ . However, even though the energy landscapes of the 3-regular graphs appear less complex and easier to navigate than their complete graph counterparts, the local minima in their energy landscapes give rise to a larger range of  $p(|s\rangle)$ . Hence a greater proportion of local minima with high energies possess low Max-Cut probabilities. This trend is captured by comparing  $F$  values between the 3-regular graphs and the complete graphs  $K_6$  and  $K_8$ , where the former graphs typically have much higher  $F$  values than the latter.

Comparing  $F$  values among the 3-regular graphs, we observe that graphs **6a** and **6b** follow a smooth downward trend with increasing  $L$ , while the 8-vertex graphs tend to peak at  $L = 2$  and  $L = 3$  before decreasing, with the exception of **8d**, which follows a similar trend of the 6-vertex graphs. The performance of the 8-vertex graphs at  $L = 2$  and  $L = 3$  can be attributed to an increase in the number of local minima with low Max-Cut probabilities that outweigh the general improvement in HCMPs and low-lying minima, while for graph **8d** this effect is reversed, with an increase in HCMPs and minima with good probabilities. At  $L = 4$ , a greater proportion of minima with high  $p(|s\rangle)$  appear for all 3-regular graphs, and we therefore recommend a minimum of  $L = 4$  when employing QAOA for these cases.

Another factor that supports the choice of  $L = 4$  comes from the construction of heuristic expectation thresholds that aim to identify minima with sufficiently high  $p(|s\rangle)$  values. This analysis can be carried out by finding the intercepts of the corresponding convex hulls with a suitable probability cutoff  $p_{op}$ . For the 3-regular graphs we choose  $p_{op} = 0.5$  and define the difference in  $\langle \hat{H}_C \rangle$  values from the global minimum to the two intercepts as the worst-case and best-case expectation cutoffs,  $d_1$  and  $d_2$ , respectively, where

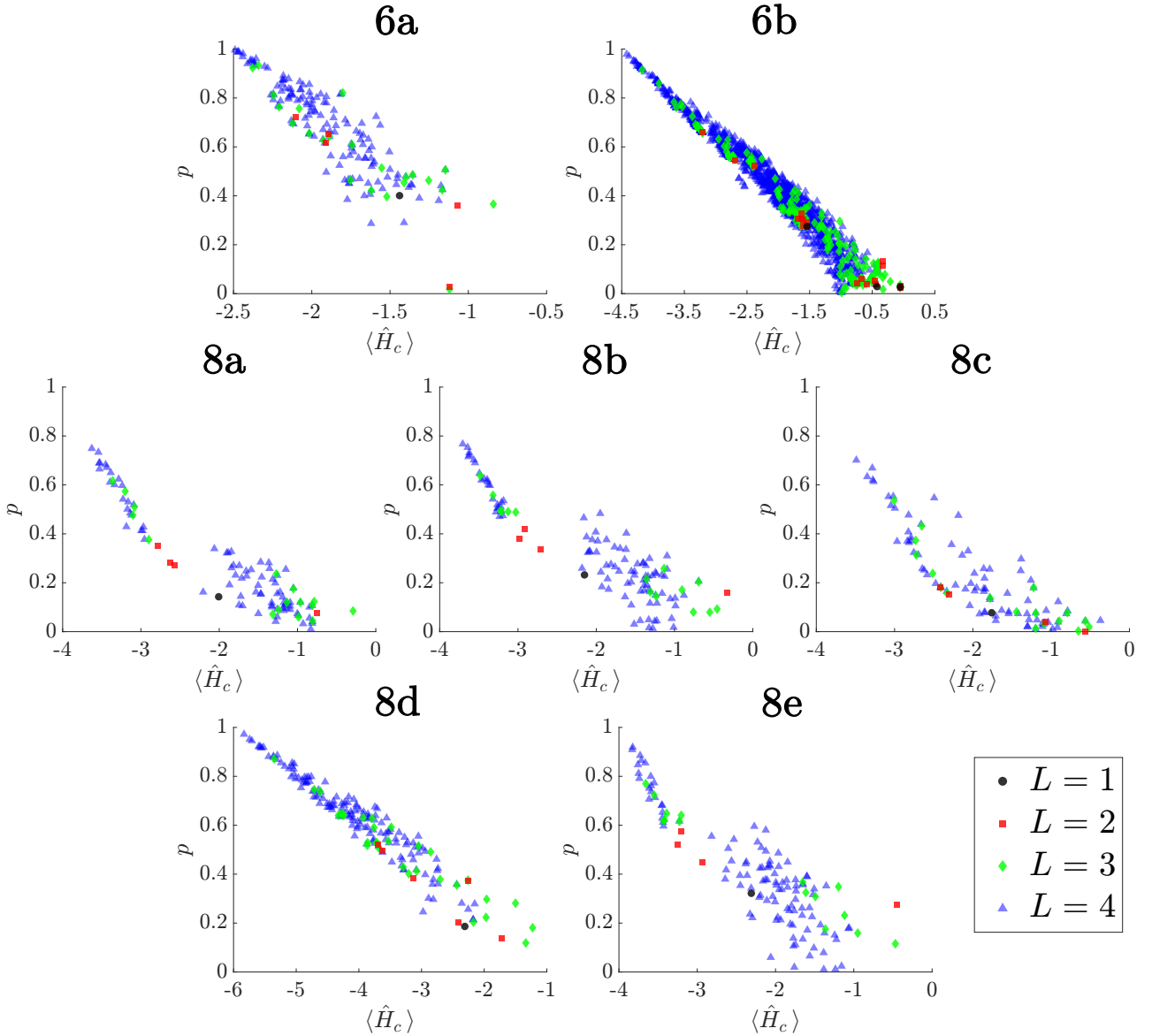


FIG. 7. Scatter plots of probabilities of the correct Max-Cut solutions against  $\langle \hat{H}_C \rangle$  for connected minima of graphs **6a–8e** for  $L = 1$  (black circle),  $L = 2$  (red square),  $L = 3$  (green diamond) and  $L = 4$  (blue triangle).

TABLE IV. Expectation thresholds  $d_1$  (top value) and  $d_2$  (bottom value) for graphs **6a–8e** of varying  $L$ .

Graph	$L = 2$	$L = 3$	$L = 4$
<b>6a</b>	0.313189	0.546894	0.578616
	0.643070	1.254700	1.342016
<b>6b</b>	0.640787	1.453239	1.660319
	0.951659	2.160089	2.470976
<b>8a</b>	-	0.215689	0.338515
	-	0.673507	1.251349
<b>8b</b>	-	0.250008	0.408135
	-	0.886500	1.652028
<b>8c</b>	-	0.046924	0.315151
	-	0.183791	1.203264
<b>8d</b>	0.052613	1.580115	1.857498
	0.202901	2.457872	2.962362
<b>8e</b>	0.096120	0.779749	0.645478
	0.731083	1.578323	1.977320

$d_1 < d_2$ . We observe that the expectation thresholds generally expand as  $L$  increases (**Table IV**), with  $d_1$  and  $d_2$  attaining their highest values at  $L = 4$ . For  $L \leq L_{min}$  the widening and stabilising of expectation thresholds is significant, along with the increase in  $M$  as  $L$  increases. We see that a greater number of minima that possess a wider range of  $\langle \hat{H}_C \rangle$  values with a sufficiently high  $p(|s\rangle)$  exist within the solution landscape for the QAOA ansatz.

### C. Competing QAOA Max-Cut solutions

Finally, we explore competing Max-Cut solutions  $|\alpha\beta\alpha\beta\rangle$  and  $|\alpha\alpha\beta\beta\rangle$  for a series of four-vertex weighted graphs with a common variable weight  $x$ , where  $x = (0, 3, 4, 5)$  correspond to the graphs  $(G_2, G_3, G_4, G_5)$ , respectively (**Fig. 8**). These graphs open up two modes of analysis: they allow comparison between  $G_2$

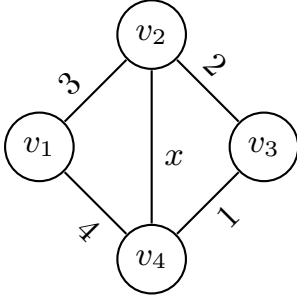


FIG. 8. Four-vertex weighted graph with a variable central weight  $x$ . The graphs  $(G_2, G_3, G_4, G_5)$  correspond to  $x = (0, 3, 4, 5)$  respectively.

TABLE V. Number of minima  $M$  (top value), HCMPs (middle value) and  $F$  (bottom value) for graphs  $G_2 - G_5$  with varying  $L$  obtained from basin-hopping global optimisation. HCMPs with asterisks indicate that they were obtained from the next highest local minimum instead of the global minimum.

Graph	$L = 1$	$L = 2$	$L = 3$
	3	16	87
$G_2$	0.477824	0.866404	0.981615
	0.594432	0.338167	0.163886
	7	109	1835
$G_3$	0.370522*	0.784475	0.948704*
	0.526539	0.300520	0.171897
	4	36	308
$G_4$	0.540426*	0.894074	1.000000
	0.461355	0.245864	0.111340
	9	183	3426
$G_5$	0.468114*	0.881732*	0.972620*
	0.498733	0.328245	0.174754

with the more complex graphs  $G_3 - G_5$ , particularly with  $G_3$ , since both sets of graphs have  $|s\rangle = |\alpha\beta\alpha\beta\rangle$ . Comparisons between  $G_3 - G_5$  can also be carried out, since  $G_5$  possesses a different correct Max-Cut solution of  $|\alpha\alpha\beta\beta\rangle$ , while for  $G_4$  both  $|\alpha\beta\alpha\beta\rangle$  and  $|\alpha\alpha\beta\beta\rangle$  are correct Max-Cut solutions. We will denote the alternative Max-Cut solution for a given graph as  $|t\rangle$ , thus for  $G_3$ ,  $|t\rangle = |\alpha\alpha\beta\beta\rangle$ ; for  $G_5$ ,  $|t\rangle = |\alpha\beta\alpha\beta\rangle$ , and  $G_4$  has no alternative solution.

We find that implementing QAOA for the weighted graphs  $G_2 - G_5$  is more difficult than for the complete unweighted graph  $K_4$ , as their energy landscapes are much more complex due to an increase in  $M$  and a decrease in their respective HCMPs (Table V). The disconnectivity graphs of  $G_2 - G_5$  exhibit similar topological features to the 3-regular unweighted graphs, possessing a well-funnelled organisation and minima featuring a wide range of  $\langle \hat{H}_C \rangle$  and Max-Cut probabilities (see Appendix D for the disconnectivity graphs of  $G_2 - G_5$  coloured based on  $p(|s\rangle)$ , and Appendix E for the disconnectivity graphs of  $G_3$  and  $G_5$  coloured based on  $p(|t\rangle)$ ). Unsurprisingly,  $G_2$  has a lower  $M$  and thus a simpler landscape than the more strained graphs  $G_3 - G_5$ , although its collection of minima with modest Max-Cut probabilities produces a comparatively high  $F$  value up to  $L = 3$ . In the

TABLE VI. Expectation thresholds  $d_1$  (top value) and  $d_2$  (bottom value) for graphs  $G_3 - G_5$  of varying  $L$ .

Graph	$L = 2$	$L = 3$
$G_3$	0.099242	0.433945
	1.124694	2.008400
$G_4$	0.489057	0.536238
	1.447505	1.722258
$G_5$	0.217591	0.459177
	1.566966	1.896063

range  $G_3 - G_5$ , it is interesting that even though  $G_5$  with a different Max-Cut solution has a more complex energy landscape than  $G_3$ , it yields a comparatively higher HCMP, while  $G_4$  exhibits the best QAOA performance as it has two distinct Max-Cut solutions. The phenomenon where the HCMP arises for the next highest local minimum rather than the global minimum was also observed for  $G_3 - G_5$ , especially for  $G_5$  (refer to Appendix B for differences in Max-Cut probabilities and  $\langle \hat{H}_C \rangle$  values between the two minima for these cases). All four graphs feature a monotonic decrease in  $F$  as  $L$  increases. Hence, as for  $K_5 - K_8$ , we recommend choosing  $L = 3$  in solving the Max-Cut problem for  $G_2 - G_5$ . Finally, it is noteworthy that for  $G_4$  and the  $L = 4$  ansatz, the number of minima greatly exceeds that of the  $L_{min} = 3$  ansatz, in contrast to the behaviour observed for  $K_5$ , highlighting the general unpredictability of the energy landscape complexity after  $L_{min}$ . For graphs  $G_3 - G_5$ , the scatter plots of the  $\langle \hat{H}_C \rangle$  values for connected minima and Max-Cut probabilities were used to construct both the convex hulls of the correct Max-Cut solution  $C_s$  and the alternative solution  $C_t$  (Fig. 9). We find that, similar to the unweighted graphs, both  $C_s$  and  $C_t$  take on more definite shapes as they become populated with more minima for increasing  $L$ . This trend allowed us to investigate  $d_1$  and  $d_2$  by finding the intercepts of  $C_s$  with the horizontal line  $p_{op}$ , setting  $p_{op} = 0.5$  for  $G_3$  and  $G_5$ , and  $p_{op} = 0.25$  for  $G_4$  (Table VI). Additionally, one may also use the intercepts between  $C_s$  and the left edge of  $C_t$  as expectation and threshold cut-offs to identify higher-quality minima with a high probability of finding  $|s\rangle$  and a low probability of obtaining  $|t\rangle$ . (See Appendix F for more details.) As for the 3-regular graphs, the divergence of  $d_1$  and  $d_2$  with increasing  $L$  makes  $L = 3$  a good choice for graphs  $G_3 - G_5$ .

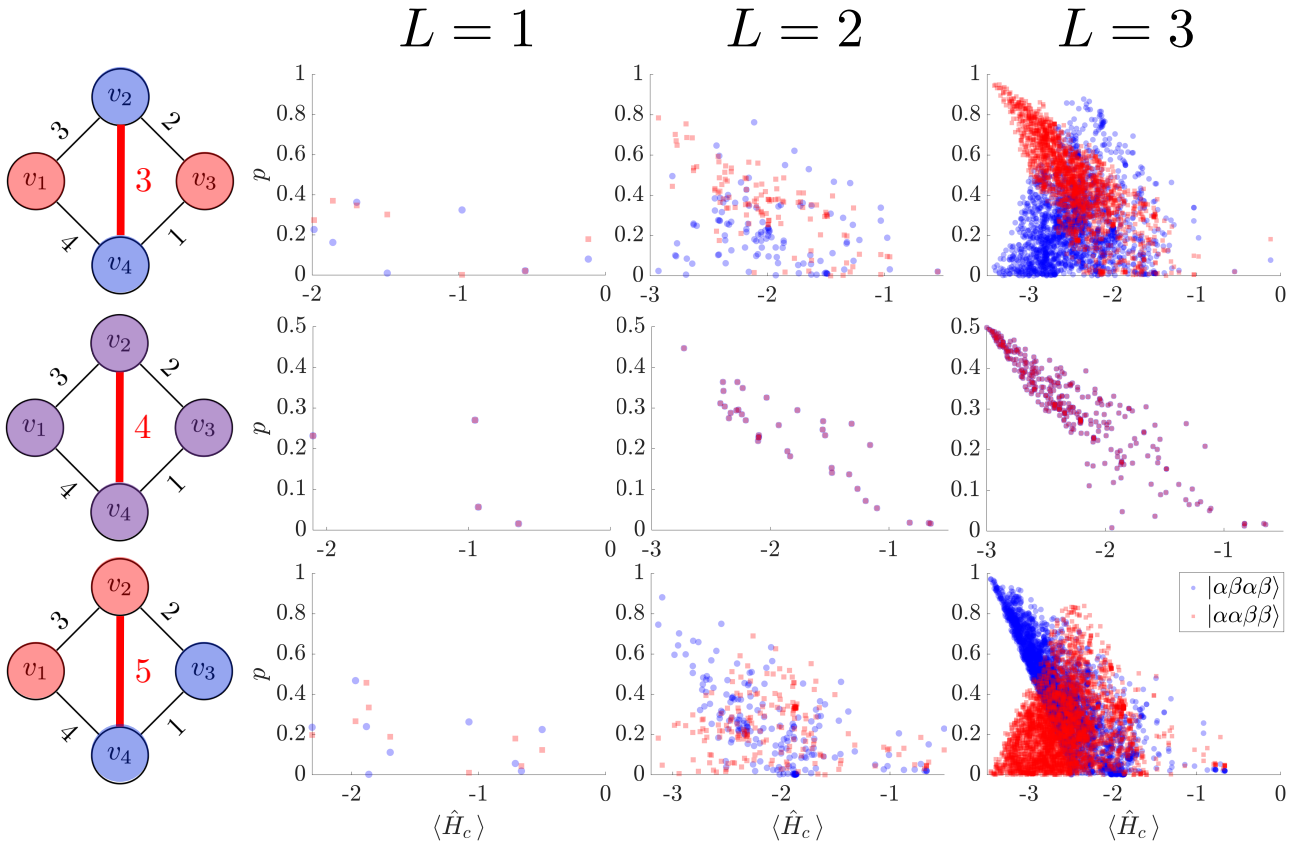


FIG. 9. Scatter plots of probabilities of competing Max-Cut solutions  $|\alpha\beta\alpha\beta\rangle$  (red square) and  $|\alpha\alpha\beta\beta\rangle$  (blue circle) against  $\langle \hat{H}_c \rangle$  for connected minima of graphs  $G_3$ ,  $G_4$  and  $G_5$  of varying  $L$ .

#### IV. CONCLUSION

In this work we explore the solution landscapes of QAOA ansätze applied to a variety of weighted and unweighted graphs by means of the energy landscapes framework, using disconnectivity graphs to visualise their topological features. We find that the corresponding landscapes are largely funnelled, suggesting that location of low-lying minima should not be particularly difficult. Under practical conditions when simulating QAOA on a quantum device, the optimisation regime is thus more likely to find a minimum close to the global minimum with a good correct Max-Cut solution probability. Even under the worst-case scenario where each experiment finds a different local minimum, so long as the local minimum is sufficiently close to the global minimum, a significant proportion of the number of shots per experiment will correspond to the Max-Cut solution. This result further demonstrates the robustness of QAOA in solving the Max-Cut problem.

We have also developed a weighted average metric  $F$  to evaluate the performance of QAOA ansätze from their corresponding databases of minima. This parameter allows one to choose a suitable number of circuit layers that balances the likelihood of obtaining good solution probabilities from local minima with an adequate circuit depth that minimises the impact from quantum noise.

Finally, we have established two ways in which ex-

pectation thresholds can be established to determine the cut-off for minima with high  $p(|s\rangle)$ . The solution landscapes we have characterised suggest that QAOA is a good VQA candidate to demonstrate practical quantum advantage. In future work we plan to extend these results to quantum machine learning (QML) algorithms, such as variational quantum classifiers (VQCs), which minimise a given cost function to classify data [68].

#### SOFTWARE AVAILABILITY

The GMIN, OPTIM and PATHSAMPLE programs are available for use under the Gnu General Public License. They can be downloaded from the Cambridge Landscape Database at [www-wales.ch.cam.ac.uk](http://www-wales.ch.cam.ac.uk).

## APPENDIX A: BASIN-HOPPING GLOBAL OPTIMISATION WITH GMIN

For each basin-hopping optimisation run, we performed 10,000 basin-hopping steps for the unweighted graphs  $K_3 - K_8$ , **6a**–**8e**, and for the weighted graphs  $G_2 - G_5$ , using the GMIN program for varying  $L$ . Each local minimisation had a minimum root-mean squared (RMS) gradient convergence criterion of  $1.0 \times 10^{-10}$  a.u., where the analytic gradients of the parameterised rotation gates of the cost and mixer layers of the QAOA ansatz were evaluated with the parameter-shift rule using **Eq. 7**. To accept/reject basin-hopping steps we employed a Metropolis criterion with a basin-hopping temperature of 1.0 a.u. If the minimum at step  $j$  has an expectation value  $\langle \hat{H}_C \rangle_j$  that is lower than the preceding iteration, i.e.  $\langle \hat{H}_C \rangle_j < \langle \hat{H}_C \rangle_{j-1}$ ,  $\langle \hat{H}_C \rangle_j$  then the corresponding angular coordinates  $\theta_j$  are accepted and used for the next step. If  $\langle \hat{H}_C \rangle_j \geq \langle \hat{H}_C \rangle_{j-1}$ , then  $\langle \hat{H}_C \rangle_j$  and  $\theta_j$  is accepted with a probability of  $\exp(-(\langle \hat{H}_C \rangle_j - \langle \hat{H}_C \rangle_{j-1})/kT)$ . Otherwise, the new minimum is rejected.

Basin-hopping moves were proposed by random perturbations of up to 1.0 rad for each angular coordinate in  $\theta_j$ . At the end of each run, the collection of minima that differ by at least  $1.0 \times 10^{-9}$  a.u in their  $\langle \hat{H}_C \rangle$  values were saved to provide a starting database for construction of the energy landscape using the OPTIM and PATHSAMPLE programs.

## APPENDIX B: DIFFERENCES IN MAX-CUT PROBABILITY AND EXPECTATION VALUES FOR NON-GLOBAL HCMP CASES

TABLE VII. Expectation differences  $\Delta\langle \hat{H}_C \rangle$  and Max-Cut probability differences  $\Delta p(|s\rangle)$  between the global and next highest local minima for non-global HCMP cases.

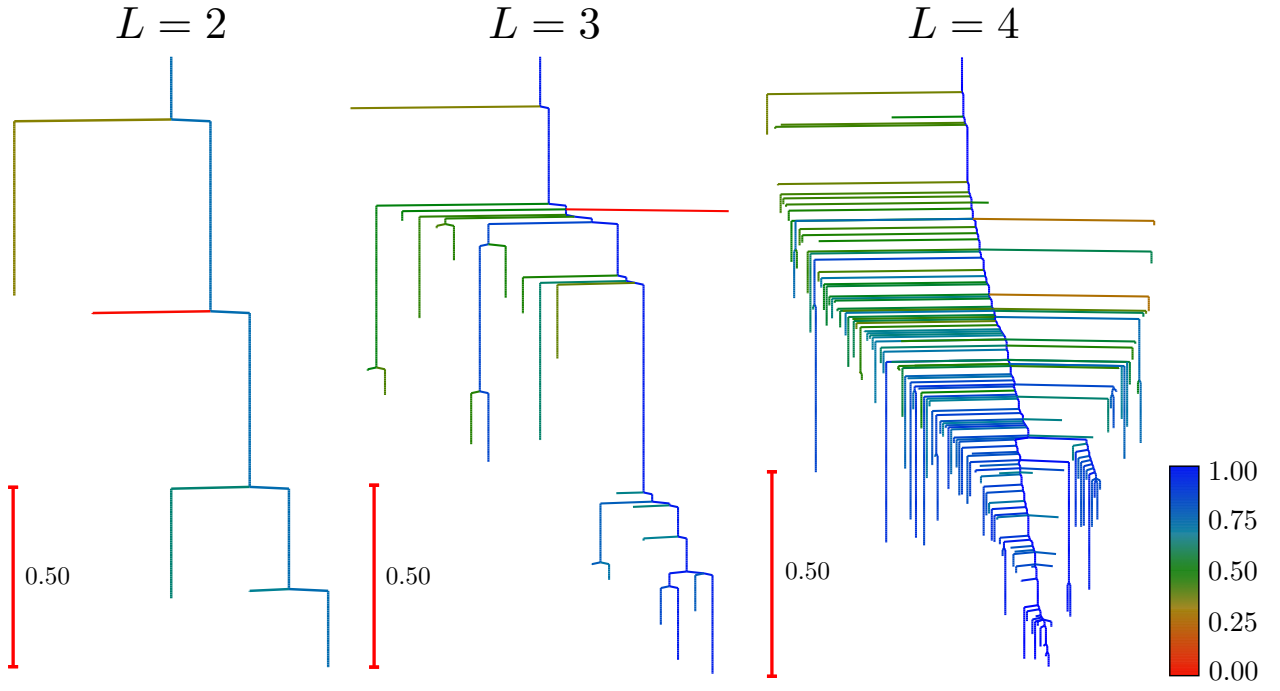
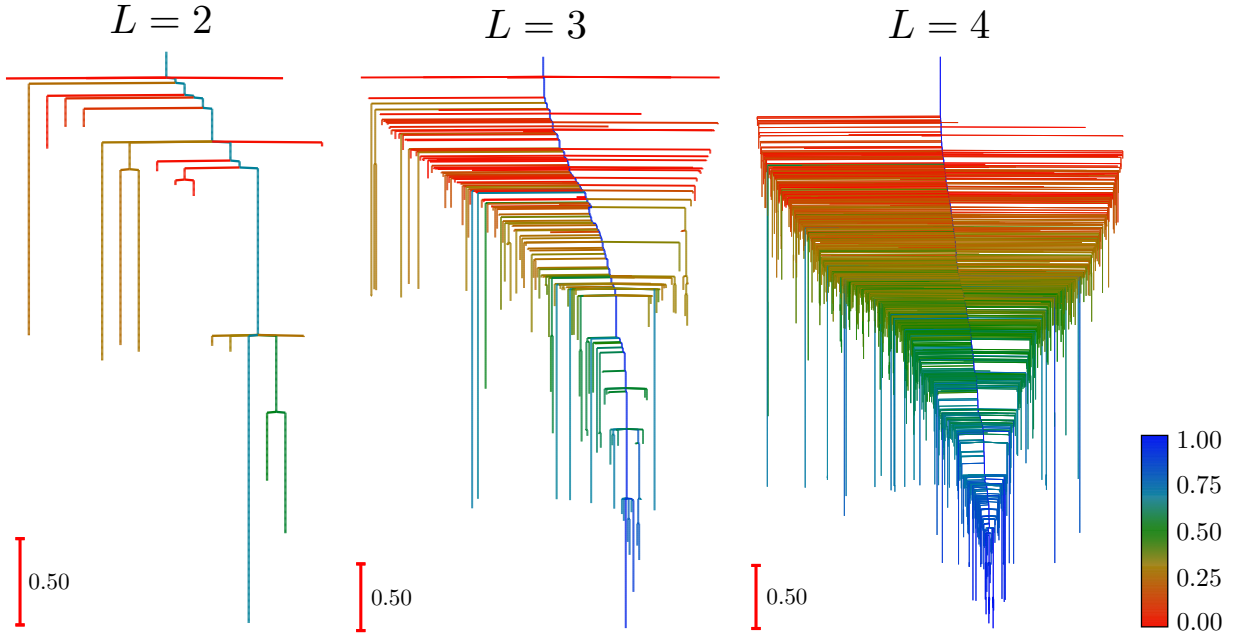
Graph	$L$	$\Delta\langle \hat{H}_C \rangle$	$\Delta p( s\rangle)$
<b>6a</b>	3	0.037856	0.010121
<b>8b</b>	2	0.075696	0.040029
<b>8e</b>	2	0.046450	0.052876
<b>8e</b>	4	0.006337	0.009846
$G_3$	1	0.127864	0.096306
$G_3$	3	0.015904	0.003739
$G_4$	1	1.142149	0.076922
$G_5$	1	0.342188	0.231787
$G_5$	2	0.036357	0.135824
$G_5$	3	0.001111	0.001329

**Table VII** shows the expectation differences  $\Delta\langle \hat{H}_C \rangle = \langle \hat{H}_C \rangle_{min} - \langle \hat{H}_C \rangle_{HCMP}$  and correct Max-Cut probability differences  $\Delta p(|s\rangle) = HCMP - p_{GM}(|s\rangle)$  for cases where the next highest local minimum has a Max-Cut probability greater than the global minimum. In general, cases with a large circuit depth  $L$  tend to have lower  $\Delta\langle \hat{H}_C \rangle$  and  $\Delta p(|s\rangle)$  as their HCMPs approach the optimal value of 1. As mentioned in the main text this phenomenon appears to

occur sporadically, as exemplified by **8e** and  $G_3$ , where it does not occur for the intermediate circuit depth of  $L = 3$ . A notable case is  $G_5$ , which features a higher Max-Cut probability in the next highest local minimum for all sampled  $L$ . We propose to investigate this phenomenon in future work to see if it arises systematically for particular classes of connected graphs.



## APPENDIX C: DISCONNECTIVITY GRAPHS OF THE 3-REGULAR GRAPHS

FIG. 10. Disconnectivity graphs for **6a** with varying circuit depth  $L$ .FIG. 11. Disconnectivity graphs for **6b** with varying circuit depth  $L$ .

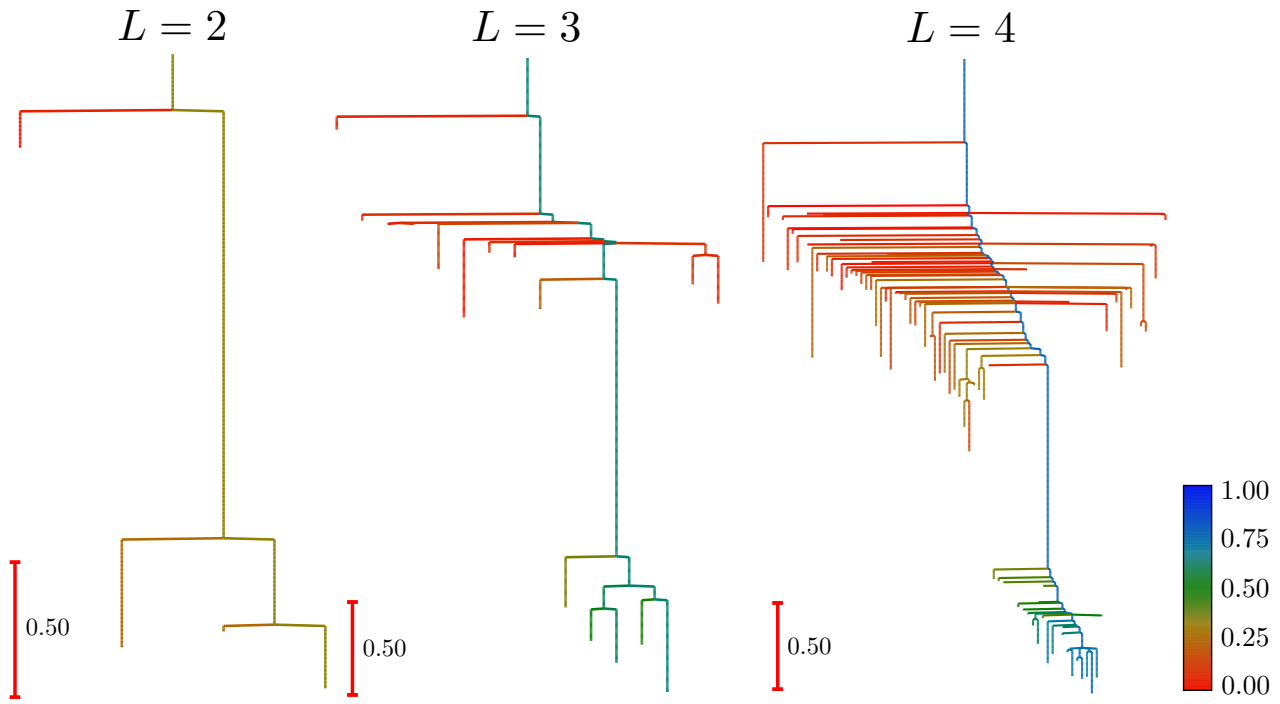


FIG. 12. Disconnectivity graphs for **8a** with varying circuit depth  $L$ .

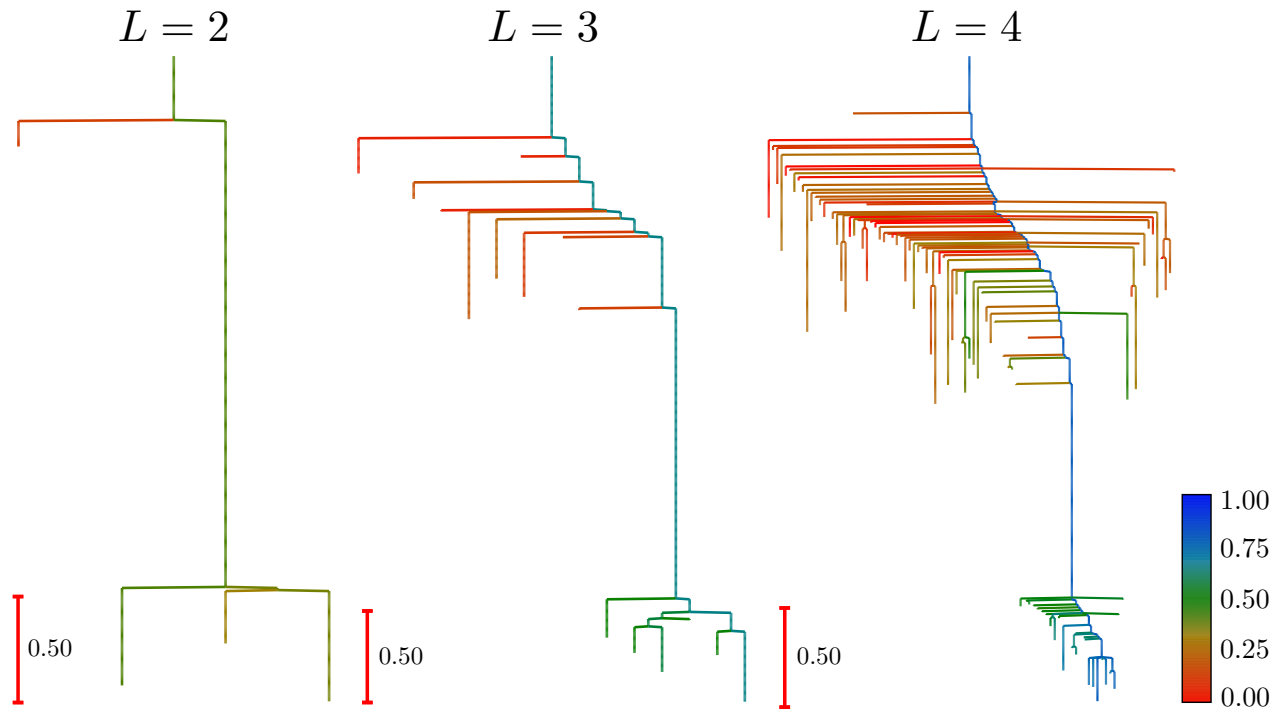


FIG. 13. Disconnectivity graphs for **8b** with varying circuit depth  $L$ .

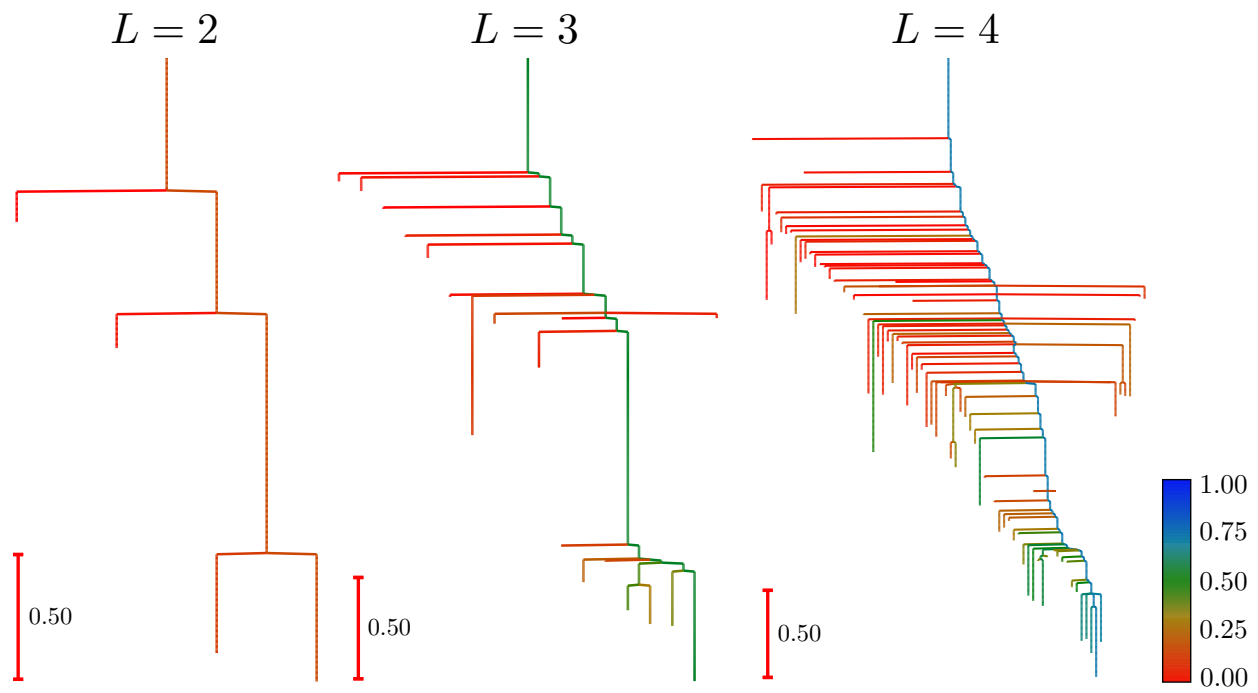


FIG. 14. Disconnectivity graphs for **8c** with varying circuit depth  $L$ .

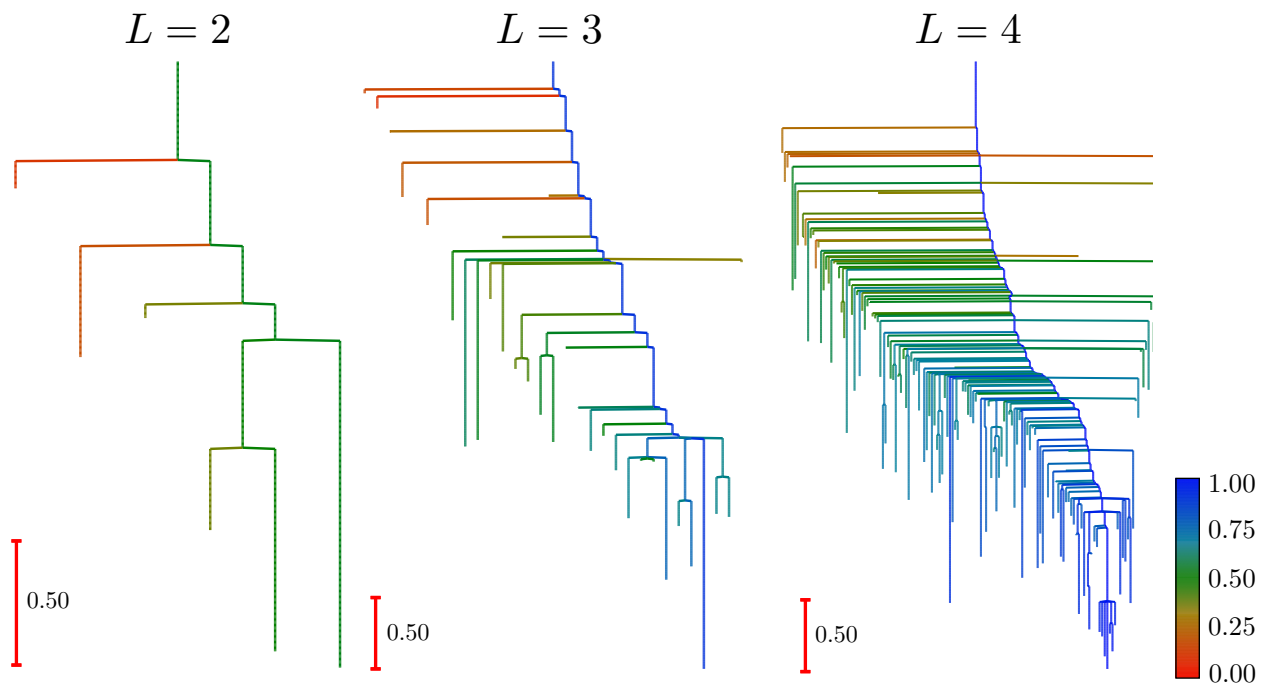


FIG. 15. Disconnectivity graphs for **8d** with varying circuit depth  $L$ .

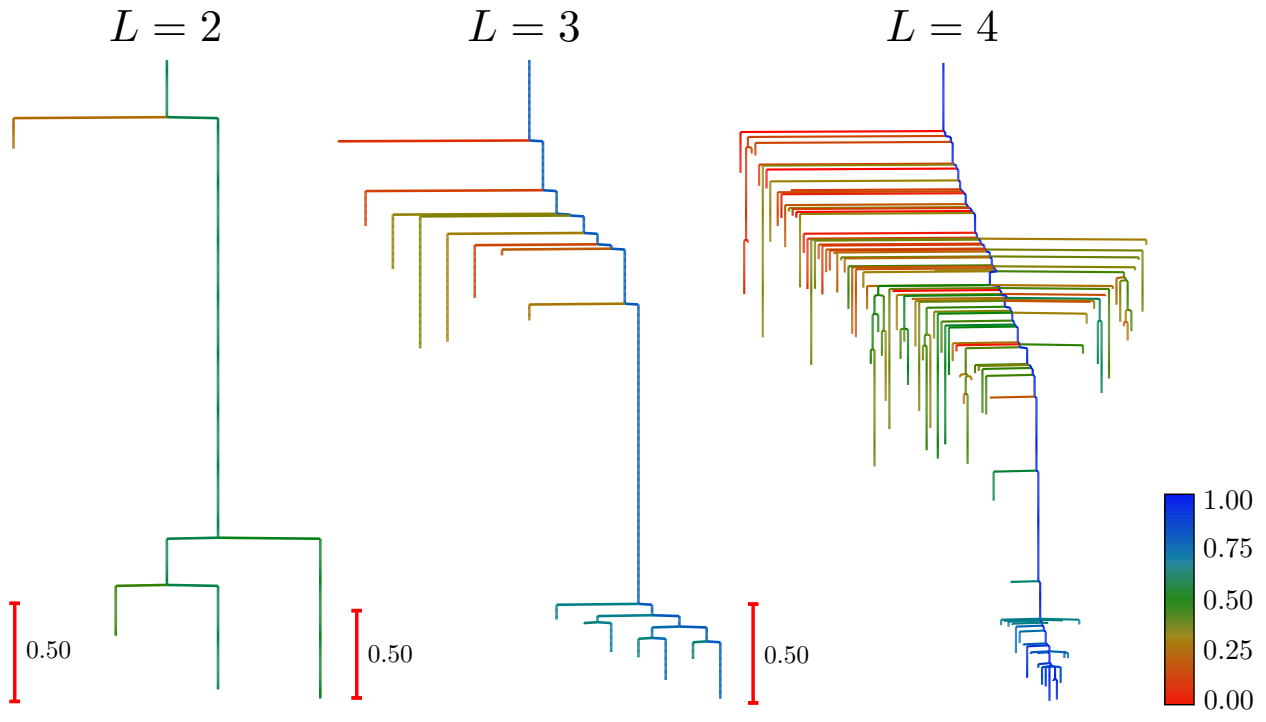


FIG. 16. Disconnectivity graphs for **8e** with varying circuit depth  $L$ .

APPENDIX D: DISCONNECTIVITY GRAPHS OF THE CORRECT MAX-CUT SOLUTIONS FOR  
 $G_2 - G_5$

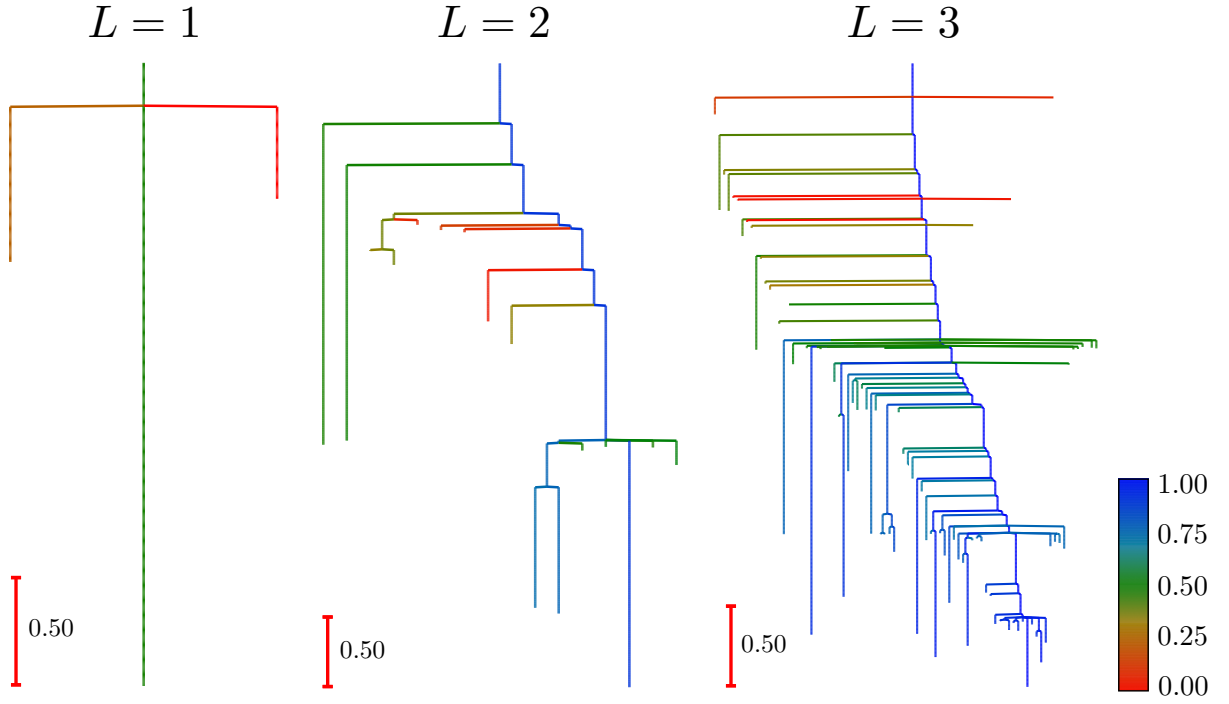


FIG. 17. Disconnectivity graphs for  $G_2$  with varying circuit depth  $L$ . Minima are coloured based on the probability of obtaining the optimal Max-Cut state of  $|\alpha\beta\alpha\beta\rangle$ .

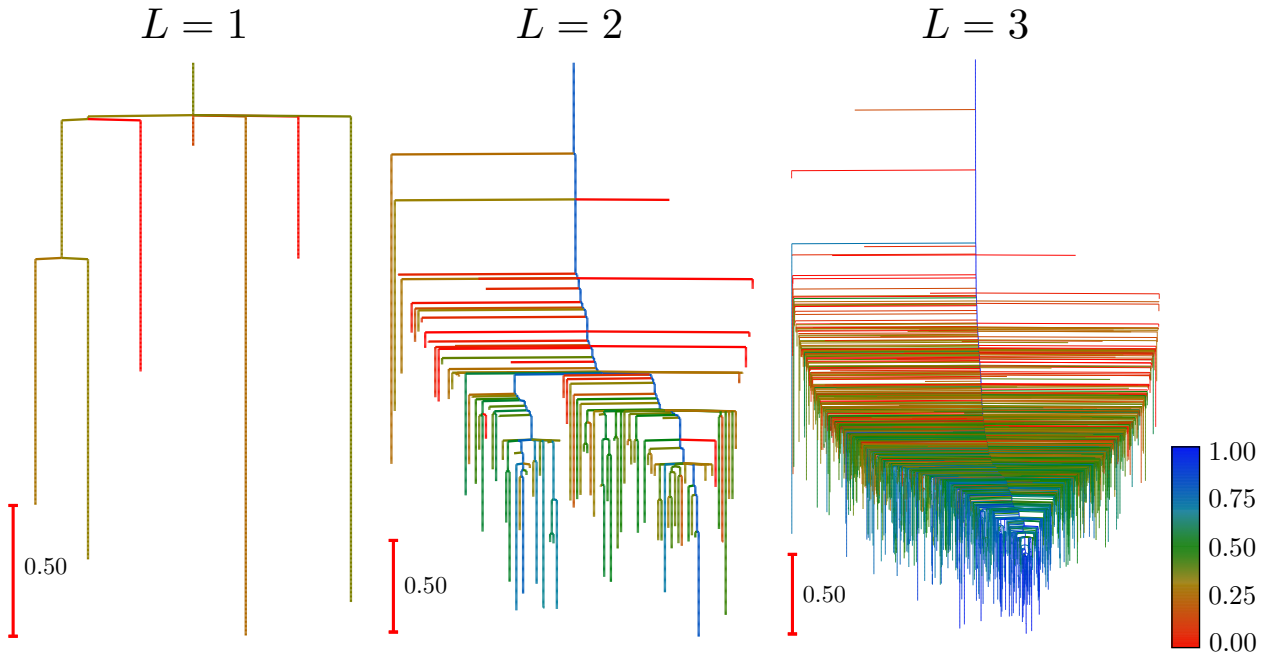
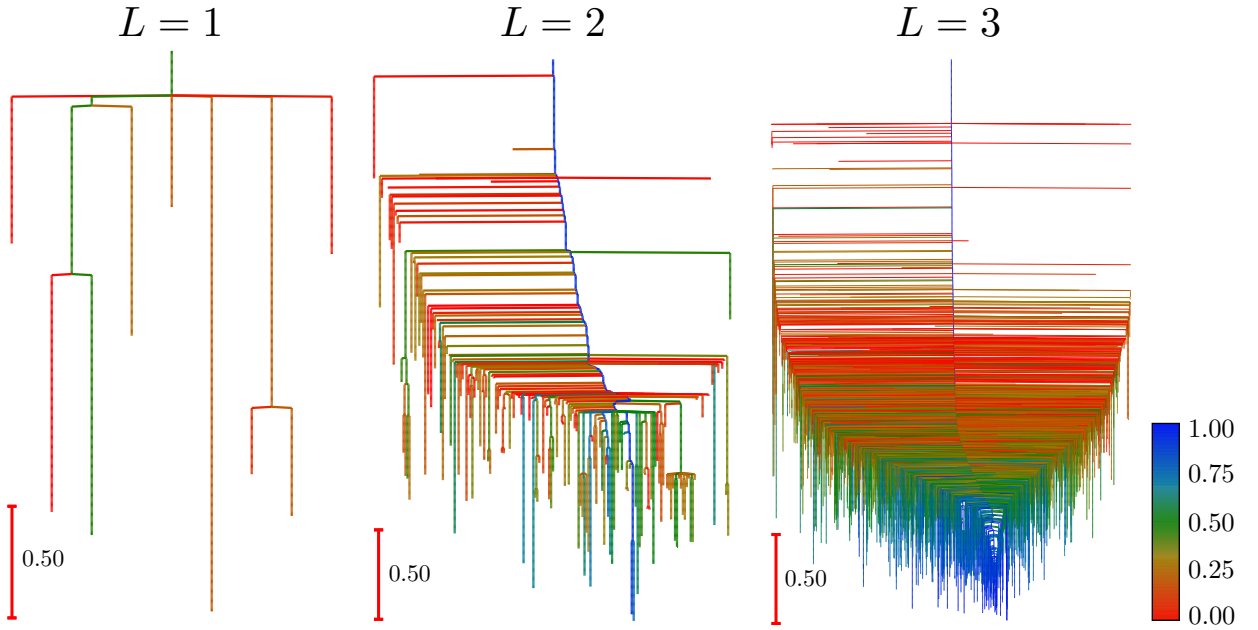
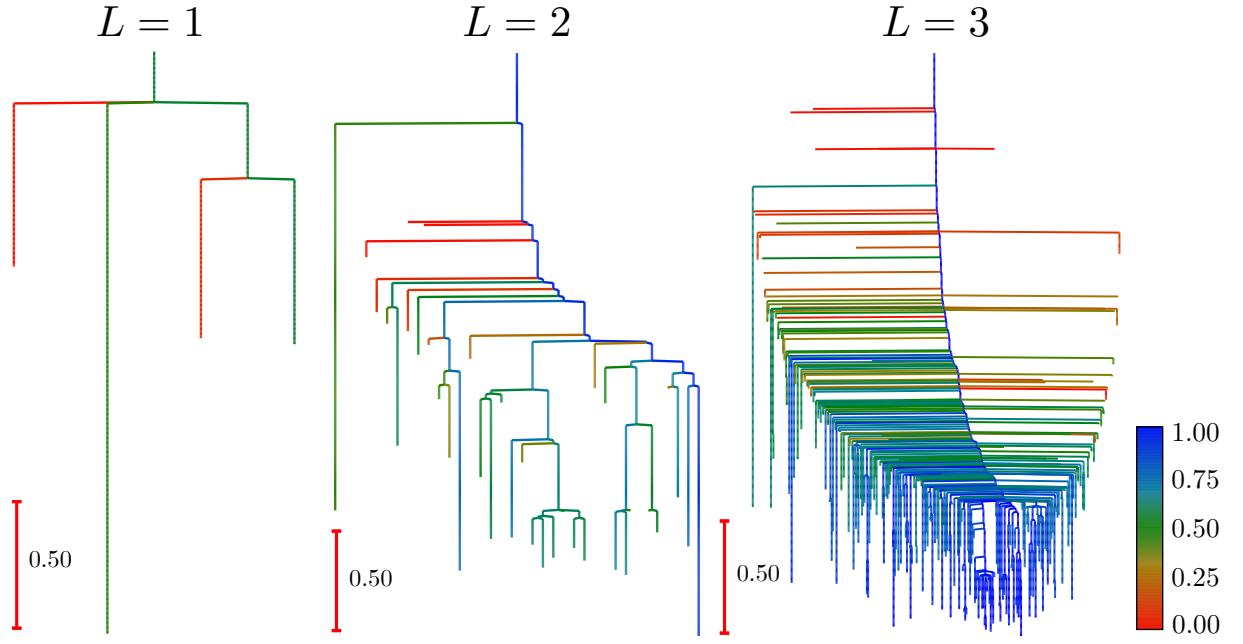


FIG. 18. Disconnectivity graphs for  $G_3$  with varying circuit depth  $L$ . Minima are coloured based on the probability of obtaining the optimal Max-Cut state of  $|\alpha\beta\alpha\beta\rangle$ .





APPENDIX E: DISCONNECTIVITY GRAPHS OF THE ALTERNATIVE MAX-CUT SOLUTIONS  
FOR  $G_3$  AND  $G_5$

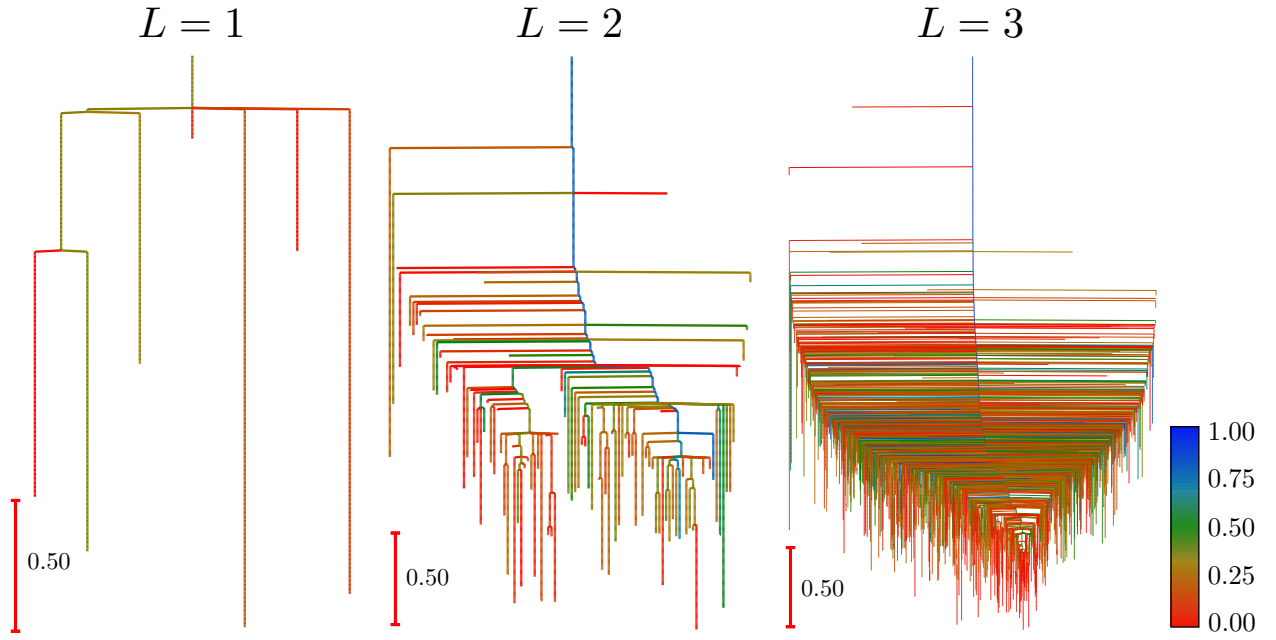


FIG. 21. Disconnectivity graphs for  $G_3$  with varying circuit depth  $L$ . Minima are coloured based on the probability of obtaining the opposing Max-Cut state of  $|\alpha\alpha\beta\beta\rangle$ .

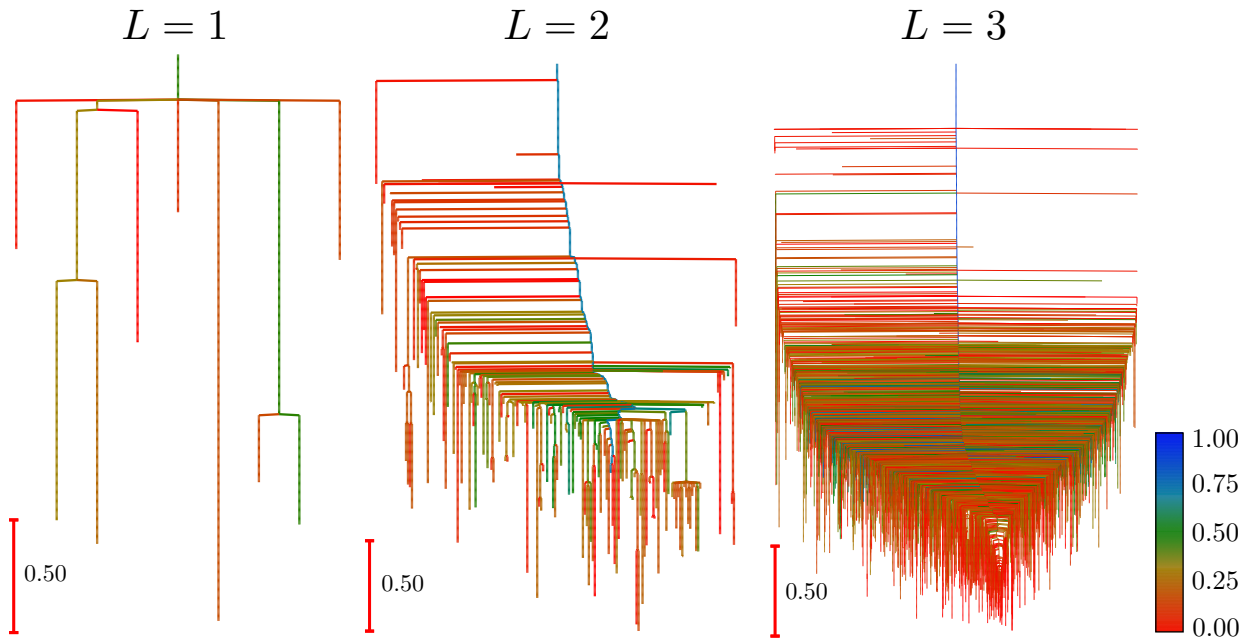


FIG. 22. Disconnectivity graphs for  $G_5$  with varying circuit depth  $L$ . Minima are coloured based on the probability of obtaining the opposing Max-Cut state of  $|\alpha\beta\alpha\beta\rangle$ .

**APPENDIX F: EXPECTATION AND  
PROBABILITY THRESHOLDS FROM THE  
CONVEX HULL INTERCEPTS FOR  $G_3$  AND  
 $G_5$**

TABLE VIII. Expectation thresholds  $d_3$  (top value) and  $d_4$  (bottom value) for graphs  $G_3$  and  $G_5$  of varying  $L$ , where  $d_3 < d_4$ .

Graph	$L = 2$	$L = 3$
$G_3$	0.111125	0.439036
	0.546385	0.794808
$G_5$	0.329259	0.476747
	0.856478	0.819369

TABLE IX. Max-Cut probability thresholds  $p_1$  (top value) and  $p_2$  (bottom value) for graphs  $G_3$  and  $G_5$  of varying  $L$ , corresponding to the expectation thresholds  $d_3$  and  $d_4$  respectively.

Graph	$L = 2$	$L = 3$
$G_3$	0.465937	0.495366
	0.665681	0.799744
$G_5$	0.373801	0.482335
	0.680284	0.790380

**Tables VIII** and **IX** summarise the two intercepts  $(\langle \hat{H}_C \rangle_{min} + d_3, p_1)$  and  $(\langle \hat{H}_C \rangle_{min} + d_4, p_2)$  of  $C_s$  with the left edge of the triangular convex hull  $C_t$  for graphs  $G_3$  and  $G_5$ , as shown in **Fig. 9**. This summary provides an alternative method to establish expectation cut-offs if additional information for alternative Max-Cut states is available. As for the expectation thresholds  $d_1$  and  $d_2$  in **Table VI**,  $d_3$  and  $d_4$  also increase with increasing  $L$ , which further justifies the choice of  $L = 3$  in refining minima within  $C_s$  that possess both good correct Max-Cut probabilities and low opposing Max-Cut probabilities. The probability cut-off of  $p_{op} = 0.5$  used in **Table VI** also appears to be situated between the probability thresholds  $p_1$  and  $p_2$ , suggesting that this choice of  $p_{op}$  is optimal.

- 
- [1] P. J. J. O'Malley, R. Babbush, I. D. Kivlichan, J. Romero, J. R. McClean, R. Barends, J. Kelly, P. Roushan, A. Tranter, and N. D. *et al.*, Scalable quantum simulation of molecular energies, *Phys. Rev. X* **6**, 031007 (2016).
- [2] F. Leymann and J. Barzen, The bitter truth about gate-based quantum algorithms in the NISQ era, *Quant. Sci. Tech.* **5**, 044007 (2020).
- [3] U. Skosana and M. Tame, Demonstration of Shor's factoring algorithm for  $N = 21$  on IBM quantum processors, *Sci. Rep.* **11**, 16599 (2021).
- [4] J. J. Burnett, A. Bengtsson, M. Scigliuzzo, D. Niepce, M. Kudra, P. Delsing, and J. Bylander, Decoherence benchmarking of superconducting qubits, *npj Quantum Inf.* **5**, 16599 (2019).
- [5] S. Chen, J. Cotler, H. Huang, and J. Li, The complexity of NISQ, *Nat. Commun.* **14**, 6001 (2023).
- [6] J. R. McClean, J. Romero, R. Babbush, and A. Aspuru-Guzik, The theory of variational hybrid quantum-classical algorithms, *New J. Phys.* **18**, 023023 (2016).
- [7] A. Peruzzo, J. McClean, P. Shadbolt, M. Yung, X. Zhou, P. J. Love, A. Aspuru-Guzik, and J. L. O'Brien, A variational eigenvalue solver on a photonic quantum processor, *Nat. Commun.* **5**, 4213 (2014).
- [8] K. Bharti, A. Cervera-Lierta, T. H. Kyaw, T. Haug, S. Alperin-Lea, A. Anand, M. Degroote, H. Heimonen, J. S. Kottmann, and T. M. *et al.*, Noisy intermediate-scale quantum algorithms, *Rev. Mod. Phys.* **94**, 015004 (2022).
- [9] X. Yuan, S. Endo, Q. Zhao, Y. Li, and S. C. Benjamin, Theory of variational quantum simulation, *Quantum* **3**, 191 (2019).
- [10] G. Ravi, K. N. Smith, P. Gokhale, A. Mari, N. Earnest, A. Javadi-Abhari, and F. T. Chong, VAQEM: A variational approach to quantum error mitigation, *IEEE*, 288–303 (2022).
- [11] K. Ito, W. Mizukami, and K. Fujii, Universal noise-precision relations in variational quantum algorithms, *Phys. Rev. Res.* **5**, 023025 (2023).
- [12] E. Fontana, N. Fitzpatrick, D. M. Ramo, R. Duncan, and I. Rungger, Evaluating the noise resilience of variational quantum algorithms, *Phys. Rev. A* **104**, 022403 (2021).
- [13] S. Halder, C. Shrikhande, and R. Maitra, Development of zero-noise extrapolated projective quantum algorithm for accurate evaluation of molecular energetics in noisy quantum devices, *J. Chem. Phys.* **159**, 114115 (2023).
- [14] A. Weidinger, G. B. Mbeng, and W. Lechner, Error mitigation for quantum approximate optimization, *Phys. Rev. A* **108**, 032408 (2023).
- [15] S. Bravyi, O. Dial, J. M. Gambetta, D. Gil, and Z. Nazario, The future of quantum computing with superconducting qubits, *J. Appl. Phys.* **132**, 160902 (2022).
- [16] Y. Kim, A. Eddins, S. Anand, K. X. Wei, E. van den Berg, S. Rosenblatt, H. Nayfeh, Y. Wu, M. Zaletel, and K. T. *et al.*, Evidence for the utility of quantum computing before fault tolerance, *Nature* **618**, 500–505 (2023).
- [17] E. Farhi, J. Goldstone, and S. Gutmann, A quantum approximate optimization algorithm (2014).
- [18] Y. Zhang, L. Cincio, C. F. A. Negre, P. Czarnik, P. J. Coles, P. M. Anisimov, S. M. Mniszewski, S. Tretiak, and P. A. Dub, Variational quantum eigensolver with reduced circuit complexity, *npj Quantum Inf.* **8** (2022).
- [19] J. Wurtz and P. J. Love, Counterdiabaticity and the quantum approximate optimization algorithm, *Quantum* **6**, 635 (2022).
- [20] G. Buonaiuto, F. Gargiulo, G. D. Pietro, M. Esposito, and M. Pota, Best practices for portfolio optimization by quantum computing, experimented on real quantum devices, *Sci. Rep.* **13** (2023).
- [21] V. Kremenetski, T. Hogg, S. Hadfield, S. J. Cotton, and N. M. Tubman, Quantum alternating operator ansatz (QAOA) phase diagrams and applications for quantum chemistry (2021).
- [22] S. Hadfield, T. Hogg, and E. G. Rieffel, Analytical framework for quantum alternating operator ansätze, *Quantum Sci. Tech.* **8**, 015017 (2022).
- [23] S. Wang, E. Fontana, M. Cerezo, K. Sharma, A. Sone, L. Cincio, and P. J. Coles, Noise-induced barren plateaus in variational quantum algorithms, *Nat. Commun.* **12**, 6961 (2021).
- [24] J. R. McClean, S. Boixo, V. N. Smelyanskiy, R. Babbush, and H. Neven, Barren plateaus in quantum neural network training landscapes, *Nat. Commun.* **9**, 4812 (2018).
- [25] M. Cerezo, A. Sone, T. Volkoff, L. Cincio, and P. J. Coles, Cost function dependent barren plateaus in shallow parametrized quantum circuits, *Nat. Commun.* **12**, 1791 (2021).
- [26] D. Wierichs, C. Gogolin, and M. Kastoryano, Avoiding local minima in variational quantum eigensolvers with the natural gradient optimizer, *Phys. Rev. Res.* **2**, 043246 (2020).
- [27] E. R. Anschuetz and B. T. Kiani, Quantum variational algorithms are swamped with traps, *Nat. Commun.* **13** (2022).
- [28] S. H. Sack, R. A. Medina, R. Kueng, and M. Serbyn, Recursive greedy initialization of the quantum approximate optimization algorithm with guaranteed improvement, *Phys. Rev. A* **107**, 062404 (2023).
- [29] E. R. Anschuetz and B. T. Kiani, Performance of the quantum approximate optimization algorithm on the maximum cut problem (2018).
- [30] D. J. Wales, *Energy landscapes* (Cambridge University Press, Cambridge, 2003).
- [31] D. J. Wales, Exploring energy landscapes, *Ann. Rev. Phys. Chem.* **69**, 401 (2018).
- [32] Z. Li and H. A. Scheraga, Monte Carlo-minimization approach to the multiple-minima problem in protein folding, *Proc. Natl. Acad. Sci. USA* **84**, 6611 (1987).
- [33] D. J. Wales and J. P. K. Doye, Global optimization by basin-hopping and the lowest energy structures of Lennard-Jones clusters containing up to 110 atoms, *J. Phys. Chem. A* **101**, 5111 (1997).
- [34] D. J. Wales and H. A. Scheraga, Global optimization of clusters, crystals and biomolecules, *Science* **285**, 1368 (1999).
- [35] D. J. Wales, Discrete path sampling, *Mol. Phys.* **100**, 3285 (2002).
- [36] D. J. Wales, Some further applications of discrete path sampling to cluster isomerization, *Mol. Phys.* **102**, 891 (2004).
- [37] B. Choy and D. J. Wales, Molecular energy landscapes of hardware-efficient ansätze in quantum computing, *J. Chem. Theory. Comput.* **19**, 1197–1206 (2023).
- [38] H. G. A. Burton, D. Martí-Dafcik, D. P. Tew, and D. J. Wales, Exact electronic states with shallow

- quantum circuits from global optimisation, npj Quantum Inf. **9** (2023).
- [39] D. J. Wales, M. A. Miller, and T. R. Walsh, Archetypal energy landscapes, *Nature* **394**, 758–760 (1998).
  - [40] T. V. Bogdan and D. J. Wales, New results for phase transitions from catastrophe theory, *J. Chem. Phys.* **120**, 11090 (2004).
  - [41] D. J. Wales, GMIN: A program for finding global minima and calculating thermodynamic properties from basin-sampling, <https://www-wales.ch.cam.ac.uk/GMIN/> (2023), accessed 1 December 2023.
  - [42] A. Mari, T. R. Bromley, and N. Killoran, Estimating the gradient and higher-order derivatives on quantum hardware, *Phys. Rev. A* **103**, 012405 (2021).
  - [43] C. G. Broyden, The convergence of a class of double-rank minimization algorithms 1. General considerations, *J. Inst. Math. Appl.* **6**, 76 (1970).
  - [44] R. Fletcher, A new approach to variable metric algorithms, *Comput. J.* **13**, 317 (1970).
  - [45] D. Goldfarb, A family of variable metric updates derived by variational means, *Math. Comput.* **24**, 23 (1970).
  - [46] D. F. Shanno, Conditioning of quasi-Newton methods for function minimization, *Math. Comput.* **24**, 647 (1970).
  - [47] D. C. Liu and J. Nocedal, On the limited memory bfgs method for large scale optimization, *Math. Program.* **45**, 503 (1989).
  - [48] J. Nocedal, Updating quasi-Newton matrices with limited storage, *Math. Comput.* **35**, 773 (1980).
  - [49] M. L. Paleico and J. Behler, A flexible and adaptive grid algorithm for global optimization utilizing basin hopping Monte Carlo, *J. Chem. Phys.* **152**, 094109 (2020).
  - [50] F. Noé and S. Fischer, Transition networks for modeling the kinetics of conformational change in macromolecules, *Curr. Opin. Struct. Biol.* **18**, 154 (2008).
  - [51] D. Prada-Gracia, J. Gómez-Gardenes, P. Echenique, and F. Falo, Exploring the free energy landscape: From dynamics to networks and back, *PLoS Comput. Biol.* **5**, e1000415 (2009).
  - [52] D. J. Wales, Energy landscapes: some new horizons, *Curr. Opin. Struct. Biol.* **20**, 3 (2010).
  - [53] S. A. Trygubenko and D. J. Wales, A doubly nudged elastic band method for finding transition states, *J. Chem. Phys.* **120**, 2082 (2004).
  - [54] D. Sheppard, R. Terrell, and G. Henkelman, Optimization methods for finding minimum energy paths, *J. Chem. Phys.* **128**, 134106 (2008).
  - [55] G. Mills, H. Jónsson, and G. K. Schenter, Reversible work transition state theory: application to dissociative adsorption of hydrogen, *Surf. Sci.* **324**, 305 (1995).
  - [56] H. Jónsson, G. Mills, and K. W. Jacobsen, Nudged elastic band method for finding minimum energy paths of transitions, in *Classical and quantum dynamics in condensed phase simulations* (World Scientific, 1998) Chap. 16, pp. 385–404.
  - [57] G. Henkelman, B. P. Uberuaga, and H. Jónsson, A climbing image nudged elastic band method for finding saddle points and minimum energy paths, *J. Chem. Phys.* **113**, 9901 (2000).
  - [58] G. Henkelman and H. Jónsson, Improved tangent estimate in the nudged elastic band method for finding minimum energy paths and saddle points, *J. Chem. Phys.* **113**, 9978 (2000).
  - [59] L. J. Munro and D. J. Wales, Defect migration in crystalline silicon, *Phys. Rev. B* **59**, 3969–3980 (1999).
  - [60] G. Henkelman and H. Jónsson, A dimer method for finding saddle points on high dimensional potential surfaces using only first derivatives, *J. Chem. Phys.* **111**, 7010 (1999).
  - [61] Y. Kumeda, L. J. Munro, and D. J. Wales, Transition states and rearrangement mechanisms from hybrid eigenvector-following and density functional theory. application to  $C_{10}H_{10}$  and defect migration in crystalline silicon, *Chem. Phys. Lett.* **341**, 185 (2001).
  - [62] J. M. Carr, S. A. Trygubenko, and D. J. Wales, Finding pathways between distant local minima, *J. Chem. Phys.* **122**, 234903 (2005).
  - [63] E. W. Dijkstra, A note on two problems in connexion with graphs, *Numerische Math.* **1**, 269 (1959).
  - [64] O. M. Becker and M. Karplus, The topology of multidimensional potential energy surfaces: Theory and application to peptide structure and kinetics, *J. Chem. Phys.* **106**, 1495 (1997).
  - [65] M. P. Harrigan, K. J. Sung, M. Neeley, K. J. Satzinger, F. Arute, K. Arya, J. Atalaya, J. C. Bardin, R. Barends, and S. B. *et al.*, Quantum approximate optimization of non-planar graph problems on a planar superconducting processor, *Nat. Phys.* **17**, 332–336 (2021).
  - [66] G. G. Guerreschi and A. Y. Matsuura, QAOA for max-cut requires hundreds of qubits for quantum speed-up, *Sci. Rep.* **9**, 332–336 (2019).
  - [67] M. Fernández-Pendás, E. F. Combarro, S. Vallecorsa, J. Ranilla, and I. F. Rúa, A study of the performance of classical minimizers in the Quantum Approximate Optimization Algorithm, *J. Comput. Appl. Math.* **404**, 113388 (2022).
  - [68] J. Jäger and R. V. Krems, Universal expressiveness of variational quantum classifiers and quantum kernels for support vector machines, *Nat. Commun.* **14**, 576 (2023).